



TESTS

2  
2008



This is to certify that the  
dissertation entitled

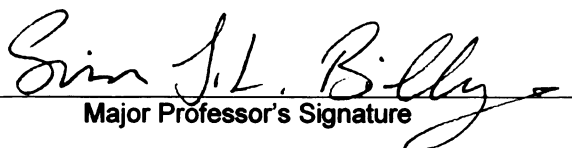
THE ROLE OF THE LOCAL STRUCTURE IN ELECTRONIC  
PROPERTIES OF VARIOUS MATERIALS

presented by

HYUNJEONG KIM

has been accepted towards fulfillment  
of the requirements for the

Ph.D. degree in PHYSICS

  
Major Professor's Signature

10/1/07

Date

**PLACE IN RETURN BOX** to remove this checkout from your record.  
**TO AVOID FINES** return on or before date due.  
**MAY BE RECALLED** with earlier due date if requested.

DATE DUE	DATE DUE	DATE DUE

THE ROLE OF THE LOCAL STRUCTURE IN ELECTRONIC PROPERTIES  
OF VARIOUS MATERIALS

By

Hyunjeong Kim

A DISSERTATION

Submitted to  
Michigan State University  
in partial fulfillment of the requirements  
for the Degree of

DOCTOR OF PHILOSOPHY

Department of Physics

2007



TH

The

stru

300

3-

str

tr

an

ri

in

P

P

t

a

a

s

v

c

s

s

a

# ABSTRACT

## THE ROLE OF THE LOCAL STRUCTURE IN ELECTRONIC PROPERTIES OF VARIOUS MATERIALS

By

Hyunjeong Kim

The *atomic pair distribution function* (PDF) technique is used to study the local structure of CeTe<sub>3</sub> in the incommensurate charge density wave (IC-CDW) state at 300 K to understand the true nature of its IC-CDW and the local structure of a  $\beta$ -Zn<sub>4</sub>Sb<sub>3</sub>, well known for a phonon-glass thermoelectric material, to search for the structural origin of its very low thermal conductivity. The PDF is obtained via Fourier transformation of neutron or x-ray powder diffraction data that include both Bragg and diffuse intensities. Having long been used to study liquids and amorphous materials, now the PDF technique is frequently applied to highly crystalline materials to investigate structural defects and disorders that play an important role in fascinating properties of modern complex materials.

The local structure of CeTe<sub>3</sub> in the IC-CDW state has been obtained using the PDF analysis of x-ray diffraction data. Local atomic distortions in the Te-nets due to the CDW are larger than observed crystallographically, resulting in distinct short and long Te-Te bonds. Observation of different distortion amplitudes in the local and average structures are explained by the discommensurated nature of the CDW since the PDF is sensitive to the local displacements within the commensurate regions whereas the crystallographic result averages over many discommensurated domains. The result is supported by STM data. This is the first quantitative local structural study within the commensurate domains in an IC-CDW system.

A study of the local atomic structure of the promising thermoelectric material  $\beta$ -Zn<sub>4</sub>Sb<sub>3</sub>, using the PDF analysis of x-ray and neutron diffraction data, suggests that the material is nanostructured. The *local* structure of the  $\beta$ -phase closely resembles

tha  
be  
con  
ph  
 $\approx$   
im

that of the low-temperature  $\alpha$  phase, the crystallographic structure of the  $\beta$ -phase being an average over different local domains of  $\alpha$ -like structure. The  $\alpha$  structure contains ordered zinc interstitial atoms which are not long-range ordered in the  $\beta$ -phase. A rough estimate of the domain size from a visual inspection of the PDF is  $\lesssim 10$  nm. It is probable that the nano-scale domains found in this study play an important role in the exceptionally low thermal conductivity of  $\beta$ -Zn<sub>4</sub>Sb<sub>3</sub>.

To my father, Young-Ho Kim

# Acknowledgments

It is very pleasure to express my deep appreciation to all members of condensed matter group at Michigan State University. I felt so fortunate to be the part of this wonderful research group.

My sincere thanks go to Prof. Simon J. L. Billinge for his generosity, encouragement, patience, and inspiration. He has taught me a lot to become a competent researcher providing so many invaluable opportunities. I can never thank him enough. Thank you very much, Prof. Billinge!

I would like to extend my deepest thanks to collaborators, Prof. Mercouri G. Kanatzidis, Prof. Stuart Tessmer, Prof. Sossina M. Haile, Prof. G. Jeffrey Snyder, Christos D. Malliakas, and Aleksandra T. Tomić. Without them these works would not have been completed.

I would like to express my great appreciation to my committee members, Prof. Vladimir Zelevinsky, Prof. Mercouri G. Kanatzidis, Prof. Stuart Tessmer, and Prof. Michael Moore for their careful review and advice on this thesis. I also would like to greatly thank Dr. Emil S. Božin for his tremendous help and patience during this Ph.D. study.

Special thanks go to Prof. S. D. Mahanti and Prof. Phillip Duxbury for their help and encouragement. I would like to thank to all of current and former group members, Dr. Pavol Juhas, Dr. Gianluca Paglia, Dr. Jacques Bloch, Dr. Xiangyun Qiu, Dr. Ahmad Masadeh, Dr. Moneeb T. Shatnawi, Dr. Mouath G. Shatnawi, and Dr. He Lin for their help and useful discussion.

Equal thanks go to Debbie Simmons and Cathy Cords who take care of so many things during my stay in Michigan State University. I also would like to acknowledge Dr. Douglas Robinson, Dr. Didier Wermeille, and Dr. Thomas Proffen for help with experiments.

I would like to give my best thank to my friends who encourage me from a long

distance. They are Eun-Young Kim, Soo-Hee Kim, Hee-Bong Lee, Soo-Kyung Chin, Jong-In Kim, Ji-Sun Kim, Sang-Hee Cho, Kang-Ae Lee, Asel Sartbaeva, and Monica Dapiaggi. Especially I would like to thank Hyo-In Park who has been my biggest supporter and critics.

Most of all, I would like to express my infinite thanks to my family who has given me endless support. I could not have stood here without them.

The work at MSU was supported from National Science Foundation through NIRT grant DMR-0304391. X-ray data were collected at the 6IDD beam-line Advanced Photon Source (APS). Use of the APS is supported by the U.S. DOE under Contract No. W-31-109-Eng-38. The MUCAT sector at the APS is supported by the U.S. DOE under Contract No. W-7405-Eng-82. The work has benefited from the use of NPDF at the Lujan Center at Los Alamos Neutron Science Center, funded by DOE Office of Basic Energy Sciences and Los Alamos National Laboratory funded by Department of Energy under Contract No. W-74050ENG-36. The upgrade of NPDF has been funded by NSF through Grant No. DMR00-76488.

# Contents

<b>1</b>	<b>Introduction</b>	<b>1</b>
1.1	Structure property relationship . . . . .	1
1.1.1	Average vs local structure . . . . .	2
1.1.2	Importance of local structural studies . . . . .	4
1.2	Charge Density Waves . . . . .	4
1.2.1	Origin . . . . .	5
1.2.2	Commensurate and incommensurate CDWs, and discommensuration . . . . .	9
1.2.3	CDW state in complex materials . . . . .	11
1.3	Thermoelectricity . . . . .	13
1.3.1	Origin . . . . .	13
1.3.2	High $ZT$ materials: Structure and thermoelectric properties .	16
1.3.3	Nanostructured thermoelectric materials: $ZT > 2$ . . . . .	18
1.4	Thesis layout . . . . .	24
<b>2</b>	<b>The Atomic Pair Distribution Function Technique</b>	<b>25</b>
2.1	The atomic Pair Distribution Function . . . . .	25
2.2	PDF as a technique of choice . . . . .	28
2.3	Obtaining the experimental PDF . . . . .	28
2.3.1	X-ray powder diffraction . . . . .	32
2.3.2	Rapid Acquisition Pair Distribution Function (RAPDF) technique . . . . .	36
2.3.3	Neutron powder diffraction . . . . .	36
2.4	Data processing, analysis, and modeling . . . . .	39
2.4.1	RAPDF data processing . . . . .	39
2.4.2	Neutron data processing . . . . .	40
2.4.3	Structural modeling . . . . .	40
<b>3</b>	<b>Local structure of CeTe<sub>3</sub> in Charge Density Wave state</b>	<b>43</b>
3.1	Introduction . . . . .	43
3.1.1	Discommensurations in IC-CDW . . . . .	44
3.1.2	Average structure and CDW state of CeTe <sub>3</sub> . . . . .	45
3.2	Experimental details . . . . .	46
3.3	Results . . . . .	48
3.4	Discussion . . . . .	50
3.5	Summary . . . . .	55



<b>4</b>	<b>Local Structure of <math>\text{Zn}_4\text{Sb}_3</math> in the <math>\beta</math> phase</b>	<b>57</b>
4.1	Introduction . . . . .	57
4.1.1	Origin of high $ZT$ and phase transitions in $\text{Zn}_4\text{Sb}_3$ . . . . .	57
4.1.2	Proposed structural models for $\beta\text{-Zn}_4\text{Sb}_3$ . . . . .	60
4.2	Experimental details . . . . .	61
4.2.1	Experiment and data process . . . . .	61
4.2.2	Structural Modeling . . . . .	64
4.3	Results . . . . .	65
4.3.1	Local structure of $\text{Zn}_4\text{Sb}_3$ in $\alpha$ -phase . . . . .	65
4.3.2	Local structure of $\text{Zn}_4\text{Sb}_3$ in $\beta$ -phase . . . . .	67
4.4	Discussion . . . . .	71
4.4.1	What is in the $\alpha$ -structural model? . . . . .	71
4.4.2	Domain size estimation . . . . .	72
4.4.3	Possible role of $\alpha$ -structural like nanodomains in thermal conductivity of $\beta\text{-Zn}_4\text{Sb}_3$ . . . . .	75
4.5	Summary . . . . .	77
<b>5</b>	<b>Concluding Remarks</b>	<b>78</b>
5.1	Summary . . . . .	78
5.1.1	$\text{CeTe}_3$ . . . . .	78
5.1.2	$\beta\text{-Zn}_4\text{Sb}_3$ . . . . .	79
5.2	Importance of local structures for understanding material properties .	79
5.3	Future Work . . . . .	80
5.3.1	Fluctuation effects in $\text{RETe}_3$ . . . . .	80
5.3.2	Nano-domains in $\beta\text{-Zn}_4\text{Sb}_3$ in the high $T$ region . . . . .	80
	<b>Bibliography</b>	<b>82</b>

# List of Tables

2.1	X-ray energies ( $K\alpha_1$ emission energies), wavelengths, and $Q_{max}$ values for laboratory x-ray sources. The $Q_{max}$ values are calculated with a maximum accessible scattering angle of $160^\circ$ . $\beta$ -filter elements for each source are also listed. . . . .	33
2.2	Refined structural parameters for Ni. The neutron PDF was obtained at 300 K. $Q_{max}$ of $27 \text{ \AA}^{-1}$ was used and the refinement range was $1.5 < r < 10 \text{ \AA}$ . . . . .	41
3.1	Isotropic atomic displacement parameters ( $U_{iso}$ ) from refined three structural models. $U_{iso}$ is in the unit of $\text{\AA}^2$ . . . . .	50
4.1	Site occupancies (fraction) for various $\beta$ - $\text{Zn}_4\text{Sb}_3$ structural models based on the $R\bar{3}c$ structural framework. . . . .	61
4.2	Refined structural parameters from various models. Lattice parameters and isotropic displacement parameters ( $U_{iso}$ ) were refined for all models. The atomic coordinates (not reported here) were refined only for mixed occupancy, vacancy and interstitial models being constrained to keep the $R\bar{3}c$ symmetry. The refinement range was $1.5 < r < 20.0 \text{ \AA}$ . . . . .	66
4.3	Comparison of the size of defects and thermal conductivity of nanostructured thermoelectric systems and $\beta$ - $\text{Zn}_4\text{Sb}_3$ at 300 K. The thermal conductivity of ErAs nanoparticles embeded $\text{In}_{0.53}\text{Ga}_{0.47}\text{As}$ was reduced by a factor of two compared to that of $\text{In}_{0.53}\text{Ga}_{0.47}\text{As}$ . . . . .	75

T

21

# List of Figures

1.1	Various materials made of carbon atoms; (a) diamond, (b) graphite, and (c) carbon nanotubes. . . . .	1
1.2	Average vs local structure. Assume the system consists of nanoscaled domains and blue atoms are ordered in a certain direction in each domain. The local structural probing techniques resolve the ordering of blue atoms whereas the crystallography provides a somehow different structure. This figure is in color. . . . .	3
1.3	Conduction band (upper part) of a linear chain of atoms (blue circles in the lower part) with a period $a$ . At $T = 0$ the band is completely filled up to the Fermi energy $E_F$ and the corresponding conduction electron density is constant in space (blue line in the lower part). This figure is in color. . . . .	6
1.4	A one-dimensional metal is unstable against a periodic deformation of its lattice with the period of $\lambda = 2\pi/2k_F$ (blue circles in the lower part). This lattice deformation opens up a gap at the Fermi level (upper part) and consequently leads to a lowering of the electronic energy of the system. The charge density of the conduction band exhibits a periodic modulation with the same wavevector as the periodic lattice deformation (blue line in the lower part). This sinusoidally modulated charge density is called the charge density wave. This figure is in color. . . . .	7
1.5	Fermi surface of (a) non-interacting metallic chains along $\vec{c}$ direction placed parallel to each other along $\vec{b}$ direction and (b) three-dimensional free electron gas. This figure is in color. . . . .	8
1.6	Various charge density waves. Depending on band filling, (a) commensurate charge density wave or (b) incommensurate charge density wave is developed. In addition to uniform incommensurate charge density wave (b) commensurate charge density wave domains separated by domain walls (c) can also give the average incommensurate charge density wave. . . . .	10
1.7	Phase diagram of $\text{Cu}_x\text{TiSe}_2$ . Open and filled circles represent the CDW and superconducting transition temperature, respectively. The inset shows the crystal structure of $\text{Cu}_x\text{TiSe}_2$ with Cu, Ti, and Se atoms in red, blue, and orange color, respectively. At $x=0.11$ , the chemical phase boundary is reached. This figure is in color. . . . .	12

1.8	(a) Crystal structure of skutterudite where corner-shared $MX_6$ octahedra create a large void (green shaded area) at the center of the cubic cell. M and X atoms are depicted in red and blue colored circles, respectively. (b) Structure of half Heusler alloys (XYZ). Blue, red, and green circles represent X, Y, and Z atoms, respectively. (c) Crystal structure of the Type I clathrate. Atoms that form a framework structure are in blue and guest atoms are in orange and purple. This figure is in color. . . . .	17
1.9	(a) Crystal structure of $Tl_9BiTe_6$ . Tl atoms are in dark blue and Te atoms in light blue. Bi and Tl mixed site (4c) are in orange. (b) Structure of $CsBi_4Te_6$ . Yellow, blue, and green circles are Te, Bi, and Cs atoms, respectively. This figure is in color. . . . .	19
1.10	$ZT$ values of high $ZT$ bulk materials; $CsBi_4Te_6$ (black filled squares), $\beta$ - $K_2Bi_8Se_{13}$ (red filled diamonds), $Tl_9BiTe_6$ (green open squares), $Bi_2Te_3$ (blue open circles), LAST (blue filled squares), LASTT (green filled diamonds), $Na_{0.95}Pb_{20}SbTe_{22}$ (red filled squares), TAGS (red open circles), PbTe (blue open diamonds), $Ce_{0.9}Fe_3CoSb_{12}$ (blue open squares), and SiGe (black open circles) are specified. This figure is in color. Reproduced with the permission of Prof. Kanatzidis. . . . .	20
1.11	$ZT$ value of 1 nm/5 nm p-type $Bi_2Te_3/Sb_2Te_3$ superlattice as a function of temperature. Notice its conspicuous thermoelectric figure of merit compared to those of other materials. . . . .	21
1.12	High resolution transmission electron microscopy image of Ag-Sb-rich nano-cluster embedded in the PbTe matrix in $AgPb_{18}SbTe_{20}$ (region enclosed by white line). The typical cluster size is 2 ~ 4 nm. . . . .	22
1.13	Compositional fluctuations between Ag, Sb, and Pb/Sn with a length-scale of ~ 3 nm (wavy pattern) in $Ag_{0.5}Pb_6Sn_2Sb_{0.2}Te_{10}$ captured by high-resolution transmission electron microscopy. $ZT$ value of ~ 1.45 was reported in this composition at 627 K. . . . .	23
2.1	(a) A two-dimensional square lattice with lattice parameter of the 2 Å and (b) the corresponding radial distribution function $R(r)$ . The first peak in $R(r)$ corresponds to correlations between the reference atom, which is crossed in red, and its nearest neighbor atoms, which coincide with the red circle in (a). The second peak is the second neighbor shell (yellow circle), and so on. This figure is in color. . . .	26
2.2	PDF provides both short and intermediate range order structural information. . . . .	29
2.3	An example of the reduced total scattering structure function $F(Q) = Q[S(Q) - 1]$ . Neutron powder diffraction data of $Ag_2O$ , which shows a huge negative thermal expansion effect, were collected at 300K. There are two pronounced features in this $F(Q)$ ; Bragg intensities which give the average structural information and diffuse intensities that provide the local deviations from the average structure. . . . .	31

2.4	The RAPDF experimental setup. It utilizes a two-dimensional image plate detector with synchrotron radiation source that overcomes the issue of long data collection time of the conventional method. The image plate is mounted orthogonally to the beam path with the beam centered on the image plate. . . . .	37
2.5	Geometry of the time-of-flight experiment setup. M, S, and D indicate a moderator, powder sample, and detector, respectively. $L_0$ is the length of the path that neutrons travel from the moderator to the sample and $L_1$ is that of scattered neutrons flight from the sample to the detector. Credit: E. S. Božin. . . . .	38
2.6	A two-dimensional image dataset from the RAPDF experiment (left). The dataset is converted to intensity vs $2\theta$ format (right). . . . .	39
2.7	Structural modeling on the experimental neutron Ni PDF obtained at 300 K. Blue open circle and red line represent the experimental and calculated PDFs, respectively. The difference between two PDFs is plotted below them (green line). This figure is in color. . . . .	42
3.1	The crystal structure of $\text{CeTe}_3$ with the square Te net where the charge density wave occurs. The reduced unit cell on the Te net is indicated by the red dashed box. This figure is in color. . . . .	45
3.2	Raw Image plate data of $\text{CeTe}_3$ at 300 K. . . . .	47
3.3	(a) The x-ray PDF of $\text{CeTe}_3$ at 300 K. (b) The first peak of the experimental PDF of $\text{CeTe}_3$ is enlarged. The shoulder due to the Peierls distortions in the Te nets is indicated by an arrow. . . . .	48
3.4	The first peak of the experimental PDF of $\text{CeTe}_3$ (blue circles) is plotted with the calculated PDF (red line) from various models: (a) the undistorted crystal structure model ( $Cmcm$ ), (b) the distorted-crystallographic model, and (c) the local structural model determined from a PDF refinement over the range $2.5 < r < 6.37 \text{ \AA}$ . The difference between the experimental and calculated PDFs is plotted below the data in each panel (green line). The shoulder due to the Peierls distortions in the Te-nets is indicated by an arrow. This figure is in color. . . . .	49
3.5	Bond-length distributions in the Te-nets refined from the PDF over various $r$ -ranges (blue line) (a) $r_{\text{max}}=6.37 \text{ \AA}$ (b) $r_{\text{max}}=6.37 \text{ \AA}$ (c) $r_{\text{max}}=14.5 \text{ \AA}$ (d) $r_{\text{max}}=27.1 \text{ \AA}$ . The $r_{\text{min}}$ value was fixed to $2.5 \text{ \AA}$ for all the cases. The bond distribution from the distorted crystallographic model (red line) is plotted in (a), (c), and (d) for comparison. In (b) the bond distribution of the local structural model ( $r_{\text{max}}=6.37 \text{ \AA}$ ) is fit with two Gaussians. The fit is shown as a red line and the two Gaussian sub-components in green lines. This figure is in color. . . .	51

71

20

3.6	(a) Gaussian like bond-length distribution is found in (b) uniform incommensurate charge density waves whereas (c) bimodal bond-length distribution is found in (d) commensurate charge density waves. The circles indicate the position of bonds in the underlying lattice and the sinusoidal waves represent the spatial distribution of conduction electron charge density. The color of the circles indicates the length of the bond; shorter bonds in dark colors and longer bonds in light colors. In the case of the uniform IC-CDW the phase of the CDW with respect to the lattice, which modulates the bond-length, varies continuously giving rise to a broad distribution of bond-lengths. In C-CDW the wave is in-phase with the lattice yielding a limited number of bond-lengths. This figure is in color. . . . .	52
3.7	(a) A representative STM image from the Te net showing the CDW. On the expanded image, the network of Te bonds is superimposed. (b) The Fourier transform of the STM data. To achieve a high signal-to-noise ratio, the transform represents the average of 24 images (each image was $27 \times 27$ nm). The unprocessed transform image shows enhanced noise along the vertical axis, an artifact due to the scan direction. This noise was removed to better resolve the peaks near the origin. The square Te net gives rise to four distinct peaks (L), with peaks related to the CDW oriented at $45^\circ$ , as indicated by the arrow. The fundamental CDW peak (corresponding to a wavelength of $\approx 15$ Å) and the $\lambda/2$ harmonic are labeled 1 and 3, respectively. Peaks 2 and 4 are in close proximity to 3, implying a characteristic discommensuration length of 38 Å, as described in the text. Peak 5 corresponds to the diagonal of the Te net. This component may be enhanced due to the underlying crystal structure; the CDW-lattice interaction may also enhance this peak. This figure is in color. . . .	54
3.8	Te-Te bond length deviation from the average value as refined crystallographically (a) and from the PDF (b). The deviation $r_{bond} - r_0$ is defined such that $r_i$ is the Te-Te bond length of the $i^{th}$ bond (bond-index $i$ ) in the unit cell and $r_0 = 3.1$ Å. (c) Schematic of the arrangements of "short" Te-Te bonds within the unit-cell coming from the PDF refinements and highlighting the formation of oligomers. Red (blue) lines and markers are "short-bonds" lying in the top (bottom) row of the unit cell. Short bonds are defined as those whose length lies within the yellow band in (b). This yellow band is centered at the position of the <i>first</i> Gaussian of the bimodal distribution in Figure ?? (b) and has a width of one standard deviation of that Gaussian. This figure is in color. . . . .	56
4.1	Temperature dependence of $ZT$ value of various thermoelectric materials.	58
4.2	Temperature dependence of thermal conductivity of various thermoelectric materials. . . . .	59



7

20

4.3	Resistance of $\text{Zn}_4\text{Sb}_3$ as a function of temperature. The inset is a zoom in the $\alpha \rightarrow \beta$ phase transition region $\sim 260$ K. . . . .	59
4.4	The crystal structure of $\text{Zn}_4\text{Sb}_3$ . (a) Project down the $c$ axis of the crystal structure of $\beta\text{-Zn}_4\text{Sb}_3$ in space group $R\bar{3}c$ . There are three distinct atomic positions, $36\text{Zn}(1)_b$ , $18\text{Sb}(1)$ , and $12\text{Sb}(2)$ . Ionic state for each site is $\text{Zn}^{2+}$ , $\text{Sb}^{3-}$ , and $\text{Sb}_2^{4-}$ in dimers for $36\text{Zn}(1)_b$ , $18\text{Sb}(1)$ , and $12\text{Sb}(2)$ , respectively. Possible Zn interstitial sites in the interstitial model are indicated with yellow small circles. (b) The interstitial atoms have full occupancy and become ordered in the $\alpha$ -phase (yellow circles). To help with comparison, only a part of a triclinic supercell is shown. This figure is in color. . . . .	60
4.5	The reduced total scattering structure function, $F(Q)$ of $\text{Zn}_4\text{Sb}_3$ obtained from neutron data at (a) 15 K ( $\alpha$ phase) and (b) 300 K ( $\beta$ phase). . . . .	62
4.6	(a) An example of a raw image data set of $\text{Zn}_4\text{Sb}_3$ obtained at 300 K and (b) $F(Q)$ for 300 K x-ray data. . . . .	63
4.7	15 K neutron PDF refinement result. (a) The experimental PDF obtained at 15 K (blue circles) together with the calculated PDF from the refined $\alpha$ -model (red line). The difference between the calculated and measured PDFs (green line) is plotted below the data. (b) Zoom in to the first PDF peak. This figure is in color. . . . .	65
4.8	300 K neutron PDF refinement results. The experimental PDF obtained at 300 K (blue circles) are plotted with the calculated PDF (red line) from various refined structural models; (a) mixed occupancy model, (b) vacancy model, (c) interstitial model, and (d) $\alpha$ -structural model. The difference (green line) is plotted below the data. This figure is in color. . . . .	68
4.9	300 K neutron PDF refinement results with fixed $U_{iso}$ value of $0.01 \text{ \AA}^2$ . The experimental PDF (blue circles) are plotted with the calculated PDF (red line) from refined (a) mixed occupancy model, (b) vacancy model, (c) interstitial model, and (d) $\alpha$ -structural model. The difference (green line) is plotted below the data. The good agreement in (d) indicates that the $\alpha$ -structural model explains the <i>local</i> structure of $\beta\text{-Zn}_4\text{Sb}_3$ with a smaller value of $U_{iso}$ whereas other models do not (a)-(c). This figure is in color. . . . .	69
4.10	Comparison of the change in PDF expected as the sample goes from the $\alpha$ to $\beta$ phase. The PDF in the $\alpha$ phase is shown in red line and the $\beta$ -phase in blue circles. The difference is plotted below in green line. (a) The <i>calculated</i> PDFs based on the average structures. $U_{iso}$ used for the calculation is $0.01 \text{ \AA}^2$ for both interstitial and $\alpha$ -structural models. (b) <i>Experimental</i> x-ray PDFs in $\beta$ (270 K, blue circles) and $\alpha$ (220 K, red line) phases. The observed changes in the local structure are much smaller than expected from the crystal structure models. This figure is in color. . . . .	70

4.11	A possible picture of $\beta$ - $\text{Zn}_4\text{Sb}_3$ structure. The structure is composed of many $\alpha$ -like domains with Zn interstitial atoms ordered along the yellow lines. (a) Local structural probes such as PDF provides $\alpha$ -like structure whereas (b) crystallography averages over domains providing three possible Zn interstitial sites with partial occupancies. This figure is in color. . . . .	73
4.12	Comparison of 15 K and 300 K PDFs in different $r$ -regions. (a) Comparison of low- (15 K, blue line) and high-temperature (300 K, red line) neutron PDFs of $\text{Zn}_4\text{Sb}_3$ plotted over a wide range of $r$ to 300 Å. (b)-(d) are the same data but plotted on expanded $r$ -scales. Note that at low- $r$ the 300 K PDF has broader and lower peaks, but at high- $r$ the situation is reversed. PDF peaks broaden with temperature due to increased thermal motion as evident at low- $r$ (b). The PDF peaks are sharper and higher at room temperature in the high- $r$ region (d) because the 300 K data are from the high-symmetry $\beta$ -phase. A rough estimate of the size of the local $\alpha$ domains can be obtained from the where the behavior switches over (c). This figure is in color. . . . .	74
4.13	The basal thermal conductivity of $1T$ - $\text{TaS}_2$ as a function of temperature. Open circles represent experimental results and dashed line is electronic contribution from Wiedeman-Franz law. Estimated lattice contribution is plotted in crosses. . . . .	76

# Chapter 1

## Introduction

### 1.1 Structure property relationship

The importance of the structure-property relationship of materials can never be emphasized enough. Even with same elemental atoms, the difference in their spatial arrangements leads to completely different properties. Good examples are diamond and graphite (Figure 1.1). Even though both of them are made of carbon atoms, they

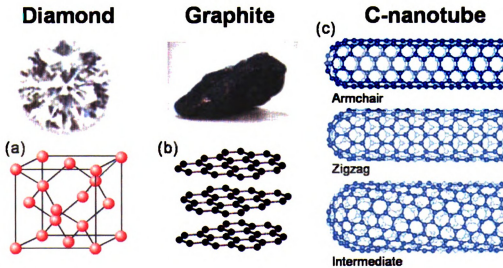


Figure 1.1: Various materials made of carbon atoms; (a) diamond, (b) graphite, and (c) carbon nanotubes.

o  
o  
o  
u  
I  
O  
t  
s  
a  
o  
th  
in  
Pa

possess completely different electronic and physical properties. Diamond is transparent, hard, and insulating, while on the contrary graphite is black, soft, and conducting. These remarkable differences arise due to the way atoms are arranged in each material, i.e. their structure. Diamond has a so called diamond structure that can be depicted as two fcc structures displaced from each other by one-quarter of a body diagonal (Figure 1.1 (a)). Graphite forms a layered structure where hexagonally structured carbon sheets are stacked perpendicular to the basal plane (Figure 1.1 (b)). Each carbon atom is covalently bonded to four other surrounding carbon atoms in the diamond structure, leading to all electrons being localized, whereas three in graphite, leading to one electron per carbon atom being delocalized. A more modern example is that of the carbon nanotube (Figure 1.1 (c)). It is a tube made of a graphene sheet (one layer of graphite) and has a diameter of close to 1 nm with a tube length many thousands of times longer. Depending on the way it is wrapped (the chirality of the tube) its bandgap varies and as a consequence its electrical property dramatically changes from metallic to semiconducting [1]. As seen from this simple example of carbon based materials, structure determination is a fundamental step towards understanding properties of any material.

### **1.1.1 Average vs local structure**

Great endeavors have been made in developing techniques to investigate the structure of materials. Among them crystallography has reigned as the most powerful structural determination tool for crystalline materials for the past century. The core assumption of crystallography is that, in crystals, arrays of atoms are repeated and ordered infinitely in space (an ideal crystal) and it greatly simplifies the problem: the spatial arrangement of only a few atoms (the asymmetric unit) must be determined. Analysis on observed Bragg peak positions and intensities in x-ray diffraction patterns specifies all the necessary information for reconstructing the structure of a

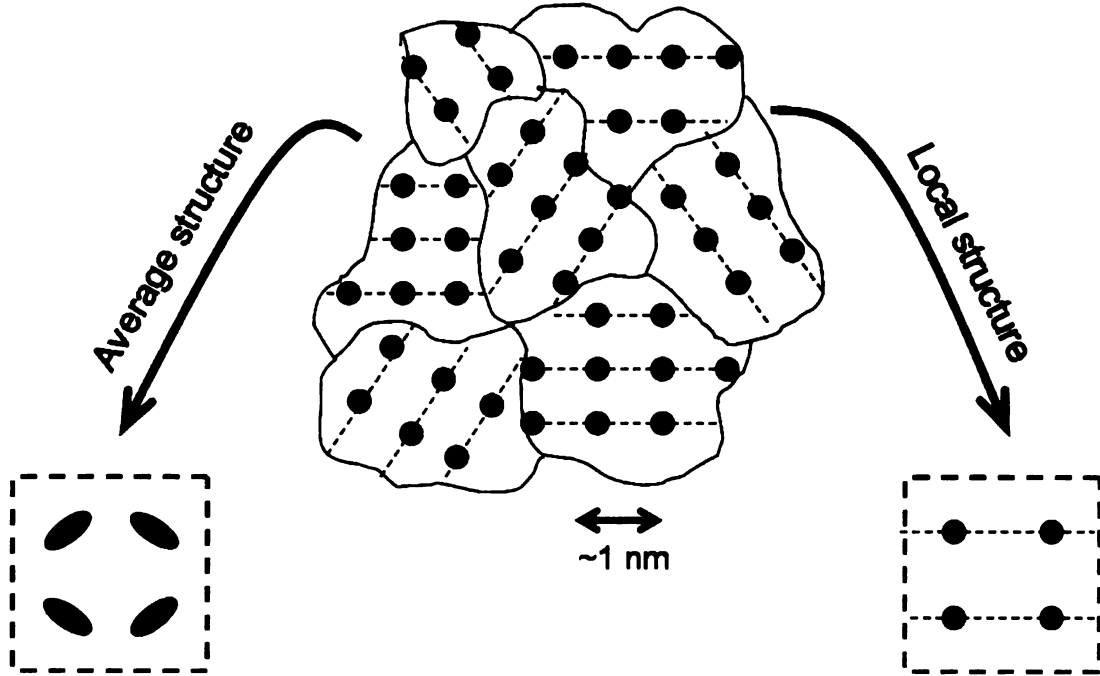


Figure 1.2: Average vs local structure. Assume the system consists of nanoscaled domains and blue atoms are ordered in a certain direction in each domain. The local structural probing techniques resolve the ordering of blue atoms whereas the crystallography provides a somehow different structure. This figure is in color.

given material, such as the atomic positions in the unit cell, atomic parameters, and symmetry elements present in the structure. However, in practice an ideal crystal does not exist due to inevitable defects and impurities and therefore long-range order extends over  $\sim 10^3$  to  $\sim 10^{20}$  atoms [2]. Imperfections in real crystals induce small perturbations of nearby atoms and therefore crystallographically determined atomic positions are the average atomic positions and the structure is often called the average structure.

There are several cases where crystallography fails. For amorphous materials, where atomic order only persists over a few atomic distances, a broad intensity distribution rather than many sharp Bragg peaks is presented in their diffraction patterns. Therefore, crystallography cannot be used and different techniques are needed that are sensitive to short range structural order. When nanoscale local ordering exists, crystallography leads to somehow different structures. For example, Figure 1.2 shows

a system consisting of many nanoscale domains. In each domain the blue atoms are ordered but the orientation of the ordering is random. Local structural probes will reveal the structure inside domains (local structure), i.e. ordering of blue atoms. On the contrary, crystallography averages over all the domains resulting in different structures, for instance, a higher symmetry structure with a large atomic displacement parameter or many possible sites with partial occupancies for blue atoms. Therefore, the average structure in this case may not explain all the electronic and physical properties of this system.

### **1.1.2 Importance of local structural studies**

Over the past few decades the field of Materials Science has been experiencing a tremendous evolution; it has been possible to design, synthesize and control new functional materials at the nanometer level. Such new complex materials, sometimes called nanostructured materials [3], are often chemically and structurally complex, and often lack long-range order or are structurally disordered. Mounting evidence suggests that their structures, defects, and interactions on nanometer length-scales are intimately connected to their remarkable properties. Therefore, in order to optimize or enhance properties, precise structural determination on the atomic scale, i.e. local structure determination is essential for nanostructured materials.

## **1.2 Charge Density Waves**

Metals with a highly anisotropic crystal and electronic structures, so called “quasi-one-dimensional” or “low dimensional”, exhibit various broken symmetry ground states: superconducting, spin density wave, and charge density wave states [4]. Among these the charge density wave state, in which translational symmetry is broken, is often found in organic and inorganic materials having linear chains or two-dimensional



layers as fundamental structural units displaying various transitions from metal to nonmetallic states.

### 1.2.1 Origin

It was Peierls (1955) who first pointed out that the one-dimensional metal is unstable against a periodic deformation of the lattice [5]. The upper part of Figure 1.3 shows the conduction band for a one-dimensional periodic array of atoms with lattice parameter  $a$  (blue circles in the lower part of Figure 1.3). At  $T = 0$  the band is filled up to the Fermi level  $E = E_F$  and the conduction electron density is uniform in space,  $\rho(r) = \rho_0$  (blue line in the lower part of Figure 1.3). It can be noticed that the electronic energy of the system can be lowered by opening up a gap at the Fermi level (the upper part of Figure 1.4). A gap at the Fermi level can be opened by introducing a periodic potential such as a periodic lattice distortion with wave vector  $\vec{k} = 2\vec{k}_F$  (blue circles in the lower part of Figure 1.4). The presence of a gap at the Fermi level modifies the dispersion relation and this leads to a position dependent conduction electron density. More specifically, the conduction electron density becomes sinusoidally modulated over space,  $\rho(r) = \rho_0 + \rho_1 \cos(2\vec{k}_F \cdot \vec{r} + \varphi)$  (blue line in the lower part of Figure 1.4) and this is called the charge density wave (CDW). The magnitude of wavevector  $\vec{k} = 2\vec{k}_F$  determines the period of the charge density wave  $\lambda = 2\pi/2k_F$ , which is same as that of the lattice distortions. The direction of the wavevector determines the direction in which the charge density wave develops. Hence the wavevector  $\vec{k} = 2\vec{k}_F$  is called CDW wavevector,  $q$ -vector, or nesting vector. It seems like the charge density wave can occur in any materials. However this is not the case. The distortions in the lattice also leads to an increase in elastic energy. For small lattice distortions  $u$ , the single-particle gap  $\Delta$  is proportional to  $u$ , the electronic energy gain is proportional to  $u^2 \ln(u)$ , and the elastic (strain) energy loss is proportional to  $u^2$  [6]. Therefore, in order to have a total energy gain, many

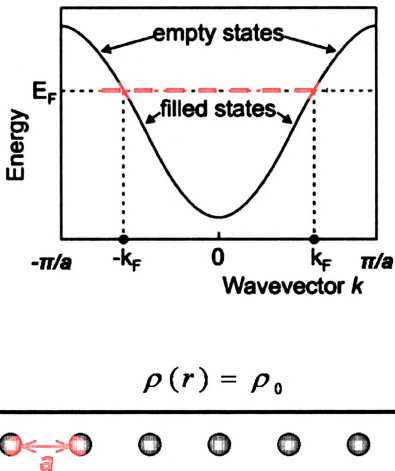
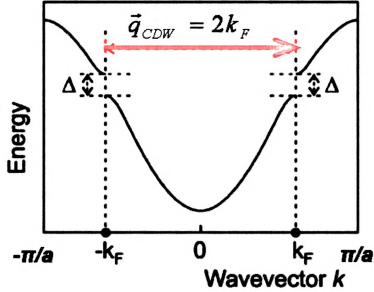


Figure 1.3: Conduction band (upper part) of a linear chain of atoms (blue circles in the lower part) with a period  $a$ . At  $T = 0$  the band is completely filled up to the Fermi energy  $E_F$  and the corresponding conduction electron density is constant in space (blue line in the lower part). This figure is in color.



$$\rho(r) = \rho_0 + \rho_1 \cos(2k_F \cdot r + \varphi)$$

The diagram shows a series of blue circles representing ions. A red sinusoidal wave is superimposed on the lattice, representing the charge density modulation. A red double-headed arrow between two peaks of the wave is labeled  $\lambda = \pi/k_F$ .

Figure 1.4: A one-dimensional metal is unstable against a periodic deformation of its lattice with the period of  $\lambda = 2\pi/2k_F$  (blue circles in the lower part). This lattice deformation opens up a gap at the Fermi level (upper part) and consequently leads to a lowering of the electronic energy of the system. The charge density of the conduction band exhibits a periodic modulation with the same wavevector as the periodic lattice deformation (blue line in the lower part). This sinusoidally modulated charge density is called the charge density wave. This figure is in color.

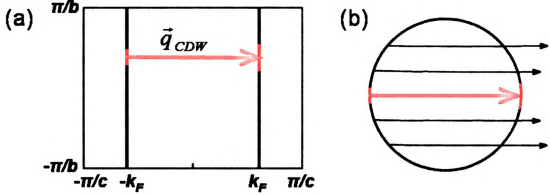


Figure 1.5: Fermi surface of (a) non-interacting metallic chains along  $\vec{c}$  direction placed parallel to each other along  $\vec{b}$  direction and (b) three-dimensional free electron gas. This figure is in color.

states on the Fermi surface should be gapped with a single CDW wavevector. For a one-dimensional metallic chain the Fermi surface consists of two points: one state at  $+k_F$  and the other at  $-k_F$  (the upper part of Figure 1.3). Both states will be gapped with a single CDW wavevector  $\vec{k} = 2\vec{k}_F$  (the upper part of Figure 1.4). The Fermi surface for non-interacting metallic chains that are placed parallel to each other along the  $\vec{b}$  direction is of two parallel lines shown in Figure 1.5 (a). In this case, each state of  $+k_F$  on the Fermi surface has a corresponding state with opposite momentum wave vector  $-k_F$  and all these paired states are separated by one nesting vector  $2\vec{k}_F$ . Therefore, the entire Fermi surface is said to be nested and will be gapped by the formation of the charge density wave. Figure 1.5 (b) shows the case for a three-dimensional free electron gas. The Fermi surface now becomes a sphere and only two states will be gapped with one wavevector (red arrow). Formation of a charge density wave is not favorable for this case. The occurrence of charge density waves depends highly on the topology of the Fermi surface of materials and the preferred topology (parallel sections of Fermi surface sheets), where many states on the Fermi surface are nested, is often found in low dimensional systems.

At finite temperature normal electrons are excited across the single-particle gap screening the electron-phonon interaction. This yields the reduction of the gap and

of the magnitude of the lattice distortion. Eventually it leads to the second-order Peierls transition at  $T_{CDW}$ . The material is a metal above the transition while it is a semiconductor below  $T_{CDW}$ .

### 1.2.2 Commensurate and incommensurate CDWs, and discommensuration

Depending on the ratio between the wavelength,  $\lambda$ , of the charge density wave and of the underlying lattice,  $a$ , charge density waves can be categorized in two ways. If  $\lambda/a$  is a rational number, the charge density wave is called a commensurate charge density wave (C-CDW). If  $\lambda/a$  is an irrational number it is called an incommensurate (IC-CDW). C-CDW and IC-CDWs are shown in Figure 1.6(a) and (b), respectively. The occurrence of C- and IC-CDW depends on band filling.

An average incommensurate charge density wave can also be formed from commensurate domains separated by domain walls called discommensurations. When the incommensurate wave vector is close to a low-order commensurate one it is referred to as nearly commensurate (NC-CDW), as shown in Figure 1.6 (c). The NC-CDW picture was first proposed by McMillan in order to explain the IC-CDW to C-CDW transition in  $2H$ -TaSe<sub>2</sub> [7, 8]. McMillan [7, 8] and Moncton *et al.* [9] noticed that the free energy of the IC-CDW could be lowered by distorting the plane wave. The energy of the CDW is lowered when it is “in phase” with the lattice. For example, if the peak of the CDW is placed between atoms, then the bond charge would be maximized gaining in bonding energy. For the uniform IC-CDW portions of the CDW will be in the proper phase with the lattice producing bonding charge whereas other portions of the CDW will be out of phase contributing to antibonding [7, 8]. Therefore, for the uniform IC-CDW the bonding energy averages out to zero. One can lower the energy by distorting the uniform CDW. One way is to modulate the phase of the CDW to increase the width of the in-phase region and decrease the width of the out-of-phase

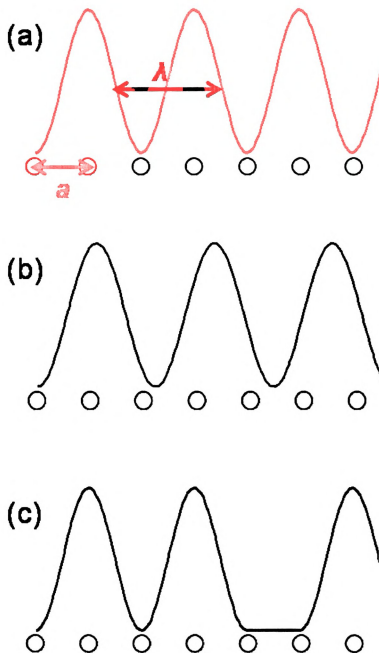


Figure 1.6: Various charge density waves. Depending on band filling, (a) commensurate charge density wave or (b) incommensurate charge density wave is developed. In addition to uniform incommensurate charge density wave (b) commensurate charge density wave domains separated by domain walls (c) can also give the average incommensurate charge density wave.

region. This will gain bonding energies at the expense of phase-modulation energy [8].

### 1.2.3 CDW state in complex materials

It has been widely believed that at low temperature the charge density wave state competes with the superconducting state [10]. Both states occur because of Fermi surface instabilities and electron-phonon coupling [11]. There are several CDW materials which are also superconducting [12, 13, 14, 15]. It was reported that applying pressure or doping a material reduced the CDW transition temperature and increased the transition temperature of the existing superconducting state. This is indicative of the competition between two states. Morosan *et al.* studied the suppression of the CDW transition in  $\text{TiSe}_2$  by intercalating Cu atoms yielding  $\text{Cu}_x\text{TiSe}_2$  [11]. They observed a new superconducting state emerging near  $x=0.04$ , with a maximum transition temperature  $T_c$  of 4.15 K at  $x = 0.08$ . The phase diagram of  $\text{Cu}_x\text{TiSe}_2$ , which resembles that of high- $T_c$  copper oxide superconductor very closely, is shown in Figure 1.7. The reason why superconductivity arises from the CDW state in  $\text{TiSe}_2$  by Cu intercalation has not yet been understood [11].

CDW states are often observed in a form of "charge ordering" in high- $T_c$  copper oxide superconductors. Both conventional CDW and superconducting transitions open up an energy gap in the single particle energy spectrum at the Fermi level but their physical properties are very different. If those two ground states coexist, they are believed to occur in different parts of Fermi surface sheets [16]. Understanding the relation between CDW and superconducting states is an important prerequisite to resolve remaining challenging issues in high- $T_c$  superconductivity [17], where the CDW state as well as spin-density-wave order/antiferromagnetism are also found. Very recently, Kiss *et al.* explored the energy and momentum distribution near the Fermi surface of a quasi-two-dimensional transition-metal dichalcogenide,  $2\text{H-NbSe}_2$  by using Angle-resolved photoemission spectroscopy (ARPES) [16].  $2\text{H-NbSe}_2$  exhibits

T

20



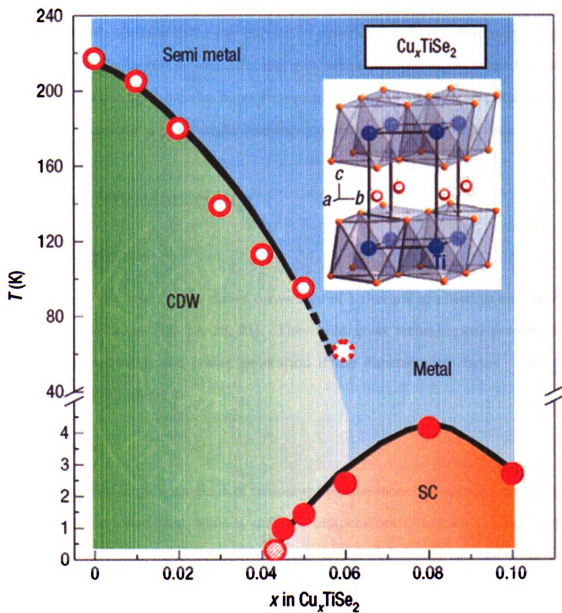


Figure 1.7: Phase diagram of  $\text{Cu}_x\text{TiSe}_2$ . Open and filled circles represent the CDW and superconducting transition temperature, respectively. The inset shows the crystal structure of  $\text{Cu}_x\text{TiSe}_2$  with Cu, Ti, and Se atoms in red, blue, and orange color, respectively. At  $x=0.11$ , the chemical phase boundary is reached. This figure is in color. Adapted from [11].

the CDW transition at  $T \sim 33$  K and the superconducting transition at  $T = 7.2$  K. In their study CDW-induced electronic structural changes were observed at specific Fermi surface crossing points in  $k$  space which were connected by the CDW wavevector obtained from neutron and x-ray diffraction experiments. Very interestingly, they also found that the largest superconducting gap were developed at the same  $k$  points concluding that charge order can boost superconductivity in an electron-phonon coupled system providing a new insight into the competing ground state picture.

## 1.3 Thermoelectricity

### 1.3.1 Origin

The thermoelectric effect is the direct conversion of a thermal gradient to an electric voltage and vice versa [18, 19, 20, 21]. They hold great technological promise for solid-state refrigeration and power generation if the dimensionless figure of merit,  $ZT$ , can be pushed above 3.

#### Seebeck effect

The Seebeck effect is the conversion of temperature differences directly into electricity. In 1821 Seebeck found that when a uniform temperature difference  $\Delta T$  was kept between two ends of a metal bar a voltage was produced between two ends [22]. He also discovered that the temperature difference between two junctions of a closed loop made of two metals could create a continuous current flow in the loop. This is because the two metals respond differently to the temperature difference. The Seebeck effect is the result of two effects: charge carrier diffusion and phonon-drag. The contribution from phonon-drag, in which phonon-electron scattering tends to push the electrons to one end of the material [23], is usually small. It is because at low temperature there are few phonons excited and at high temperature the momentum of phonons is

passed on to the phonons rather than electrons due to the increase of phonon-phonon scattering. Most of the time, the charge carrier diffusion is the dominant mechanism in the Seebeck effect. A constantly applied temperature difference between the two ends of a metal bar cause hot charged carriers to diffuse from the hot side to the cold side and cold carriers to diffuse from the cold end to the hot end. If the diffusion rate of hot and cold carriers were equal, there would be no net flux of charge [24]. However, those charge carriers are scattered by impurities, imperfections, and phonons and the energy dependent scattering will lead the hot and cold carriers to diffuse at different rates [25]. This creates a higher density of carriers at one end of the material, and produces a potential difference between the two ends. This is called the thermoelectric voltage since it is created by a temperature difference. This electric field (a potential difference), however, pushes the hot (cold) charge carriers back to the hot (cold) side. An equilibrium will be reached when the number of carriers diffusing in one direction is equal to the number of carriers moving in the opposite direction due to the induced thermoelectric voltage. For the temperature difference  $dT$  between the two ends of a metal bar the induced thermoelectric voltage is

$$dV = SdT, \tag{1.1}$$

or equivalently

$$E = S\nabla T, \tag{1.2}$$

where  $S$  is the Seebeck coefficient or thermoelectric power or thermopower, which is the measure of the magnitude of an induced voltage in response to a temperature difference across a given material. The thermopower of a material depends on impurities, imperfections, and structural changes [25]. Typically metals have small thermopowers because most of them have half-filled bands where both electrons and holes participate in the carrier diffusion process. Therefore, their contributions to the

T

20

induced thermoelectric voltage are almost equal and cancel each other making the net effect small. In contrast, semiconductors can be doped with electrons or holes and thus can have large positive or negative values of the thermopower depending on the charge of the excess carriers. Therefore, good thermoelectric materials are typically heavily doped semiconductors.

### **Peltier effect**

In 1834 Peltier found that when a constant current is made to flow through a closed loop formed of two dissimilar metals or semiconductors one junction cools off while the other heats up [26]. The Peltier effect is the reverse of the Seebeck effect and often used for thermoelectric cooling.

### **Thomson effect**

The Thomson effect is the heating or cooling of a conductor where a net electric current exists in the presence of a temperature gradient [27]. Depending on the material, any current-carrying conductor with a temperature difference between two ends will either absorb or emit heat.

### **Thermoelectric figure of merit $ZT$**

The thermoelectric performance of a given materials is measured by the thermoelectric figure of merit  $ZT$  defined

$$ZT = \frac{S^2 \sigma T}{\kappa}, \quad (1.3)$$

where  $S$ ,  $T$ ,  $\sigma$ , and  $\kappa$  denote thermoelectric power, temperature, electrical conductivity, and thermal conductivity, respectively [28]. A good thermoelectric material has a large  $ZT$  value. The materials challenge is to minimize thermal conductivity without reducing the electrical conductivity, i.e. to produce strong scattering of phonons, but not electrons. Therefore, an ideal thermoelectric material is often said

T

20

to be “phonon-glass” and “electron-crystal” [29].

### 1.3.2 High $ZT$ materials: Structure and thermoelectric properties

The excellent overview on this topic comes from the review paper by G. S. Nolas *et al* [30].

Skutterudites have a cubic structure where eight  $MX_6$  octahedra are corner-shared creating a large void at the center of the cubic lattice (Figure 1.8 (a)). This large void can be filled with a large atom (lanthanide, actinide, alkaline-earth, alkali, thallium, and Group IV elements) resulting in composition  $R_2M_8X_{24}$ , where typically  $M=Co, Rh, \text{ or } Ir$  and  $X=P, As, \text{ or } Sb$  [30]. Good thermoelectric properties of skutterudites are due to the guest atoms occupying large voids, often called “rattler” atoms. These rattler atoms act as strong phonon scattering sources greatly reducing the lattice thermal conductivity [31]; for example, only five percent of Ce introduced in  $CoSb_3$  reduces the thermal conductivity to almost a half of the value of pure  $CoSb_3$  [32]. The  $ZT$  value of  $1.2 \sim 1.4$  at 900 K was reported in  $CeFe_{4-x}Co_xSb_{12}$  [32].

Half-Heusler alloys possess a structure closely related to the structure of full Heusler alloys ( $XY_2Z$ ), which is constructed with four interpenetrating fcc sublattices mutually shifted along the body diagonal by a one-quarter distance [33]. The structure of half-Heusler alloys can be obtained by removing one of two Y sublattices from the full Heusler alloy resulting in the chemical formula  $XYZ$ , where  $X$ =transition or rare earth metal,  $Y$ =transition metal, and  $Z$ =semiconductor or non-magnetic metal atoms (Figure 1.8 (b)). Their narrow bands with heavy carrier mass, which eventually lead to a large thermopower, made them recognized as potential thermoelectric materials [33]. However, effective reduction of their high thermal conductivity is a great challenge to achieve high  $ZT$ . Sb-doped  $ZrNiSn$  alloys where Pd atoms are partially substituted in the Ni sublattice exhibit  $ZT \approx 0.7$  at 800 K [34].

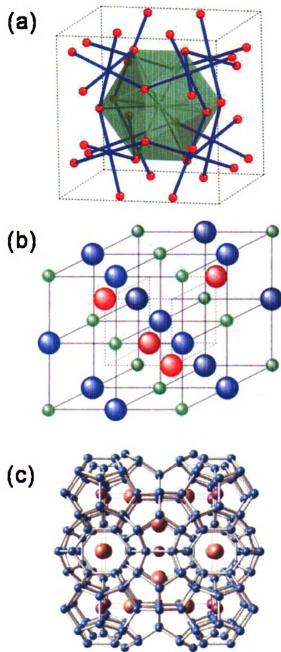


Figure 1.8: (a) Crystal structure of skutterudite where corner-shared  $MX_6$  octahedra create a large void (green shaded area) at the center of the cubic cell. M and X atoms are depicted in red and blue colored circles, respectively. Adapted from [30]. (b) Structure of half Heusler alloys ( $XYZ$ ). Blue, red, and green circles represent X, Y, and Z atoms, respectively. (c) Crystal structure of the Type I clathrate. Atoms that form a framework structure are in blue and guest atoms are in orange and purple. This figure is in color. Adapted from [30].



In clathrates, the tetrahedrally bonded unit of Ge, Si, or Sn atoms forms a framework structure creating large cages [30] (Figure 1.8 (c)). The type I group of clathrates with a general formula  $A_8^{II}B_{16}^{III}B_{30}^{IV}$ , where  $A^{II}$ =Ba or Sr,  $B^{III}$ =Al or Ga, and  $B^{IV}$ =Si, Ge, or Sn show favorable thermoelectric properties. Large-amplitude vibration of  $A^{II}$  atoms residing inside the cages of the  $B^{III}$ - $B^{IV}$  framework efficiently scatter long wavelength phonons resulting in a very low “glass-like” thermal conductivity [35]. The  $ZT$  value of 0.7 for  $Ba_8Ga_{16}Ge_{30}$  at 700 K and 0.87 for  $Ba_8Ga_{16}Si_{30}$  at 870 K are estimated from low-temperature thermal transport measurements [35].

Chalcogenide materials have been extensively studied to search for new high performance thermoelectric materials. Notable classic thermoelectric chalcogenides are  $Bi_2Te_3$  and  $PbTe$ .  $PbTe$  shows a maximum  $ZT \sim 0.8$  at around 770 K [30].  $Tl_9BiTe_6$  is one of new high  $ZT$  materials ( $ZT \sim 1.2$  at 500 K) crystalizing in a tetragonal structure (Figure 1.9 (a)) [36].  $Bi^{3+}$  and  $Tl^{1+}$  atoms are randomly distributed on the 4c site (depicted in orange circles in Figure 1.9 (a)) and this mixed valence site presumably induces strong phonon scattering resulting in the extremely low thermal conductivity of  $0.39 \text{ Wm}^{-1}\text{K}^{-1}$  at 300 K [36]. Another example is  $CsBi_4Te_6$ . It has a layered anisotropic structure composed of  $[Bi_4Te_6]^{1-}$  slabs alternating with layers of  $Cs^+$  ions (Figure fig;ch1;chalcogenides (b)) [30]. Doping with  $SbI_3$  or  $Sb$  enhances its  $ZT$  value up to 0.8 at 225 K [37]. Good thermoelectric properties below 300 K makes  $CsBi_4Te_6$  an excellent candidate for low-temperature thermoelectric applications. *ab-initio* electronic structure calculations suggest that a very narrow energy gap and a large anisotropy in the carrier effective masses play an important role in high  $ZT$  of  $CsBi_4Te_6$  [38].

### 1.3.3 Nanostructured thermoelectric materials: $ZT > 2$

In order for thermoelectric materials to be commercially applicable, such as for a thermoelectric refrigerator to be competitive with the currently available mechanical

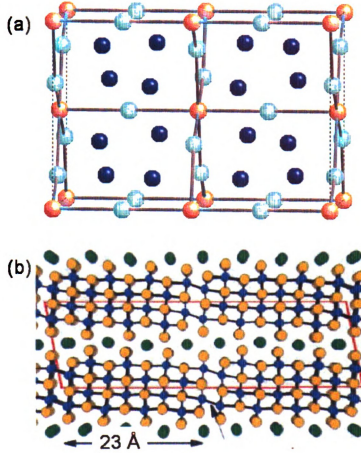


Figure 1.9: (a) Crystal structure of  $\text{Tl}_9\text{BiTe}_6$ . Tl atoms are in dark blue and Te atoms in light blue. Bi and Tl mixed site ( $4c$ ) are in orange. (b) Structure of  $\text{CsBi}_4\text{Te}_6$ . Yellow, blue, and green circles are Te, Bi, and Cs atoms, respectively. This figure is in color. Adapted from [30].

refrigerators, a figure of merit ( $ZT$ ) larger than 3 is required [39, 40]. However, it is even hard to exceed a  $ZT$  value of unity [41] (Figure 1.10). It was more than four decades ago when a material with  $ZT \sim 1$  was first reported [42]. However, despite the vigorous search for new high  $ZT$  thermoelectric materials, progress on enhancing  $ZT$  values has been slow. Quite recently new systems with  $ZT > 2$  were reported generating great excitement in the field of thermoelectrics.

Venkatasubramanian *et al.* synthesized  $\text{Bi}_2\text{Te}_3/\text{Sb}_2\text{Te}_3$  superlattices with various periods and thicknesses of the constituents to study their effects on thermal conductiv-



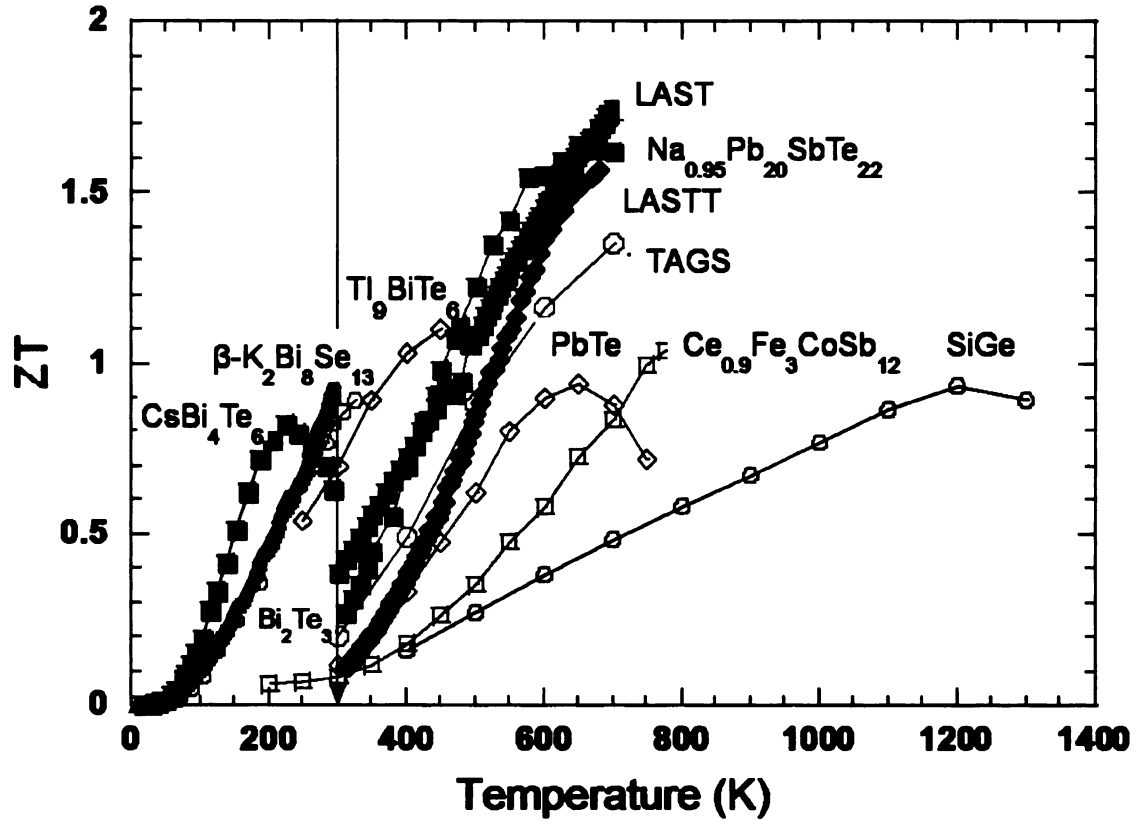


Figure 1.10:  $ZT$  values of high  $ZT$  bulk materials;  $\text{CsBi}_4\text{Te}_6$  (black filled squares),  $\beta\text{-K}_2\text{Bi}_8\text{Se}_{13}$  (red filled diamonds),  $\text{Tl}_9\text{BiTe}_6$  (green open squares),  $\text{Bi}_2\text{Te}_3$  (blue open circles), LAST (blue filled squares), LASTT (green filled diamonds),  $\text{Na}_{0.95}\text{Pb}_{20}\text{SbTe}_{22}$  (red filled squares), TAGS (red open circles), PbTe (blue open diamonds),  $\text{Ce}_{0.9}\text{Fe}_3\text{CoSb}_{12}$  (blue open squares), and SiGe (black open circles) are specified. This figure is in color. Reproduced with the permission of Prof. Kanatzidis.

ities perpendicular to the interfaces [43] and consequent  $ZT$  values [42]. The system is believed to block phonons but transmit electrons. Interestingly, thermal conductivity appears to be relatively independent of the thickness of the constituents but dependent on the period. Superlattices with a period of 5 ~ 6 nm exhibits the smallest thermal conductivity; a factor of 2 smaller than that of a  $\text{Bi}_{0.5}\text{Sb}_{1.5}\text{Te}_3$  alloy [43]. A phase-correlated phonon scattering model was proposed to explain such a low thermal conductivity of this system [43]. A consequent  $ZT$  value for the 1 nm/5 nm  $\text{Bi}_2\text{Te}_3/\text{Sb}_2\text{Te}_3$  superlattice exceeds 2 at ~ 300 K (Figure 1.11) [42].

Hsu *et al.* reported new high  $ZT$  bulk thermoelectric materials  $\text{AgPb}_m\text{SbTe}_{2+m}$  [44].

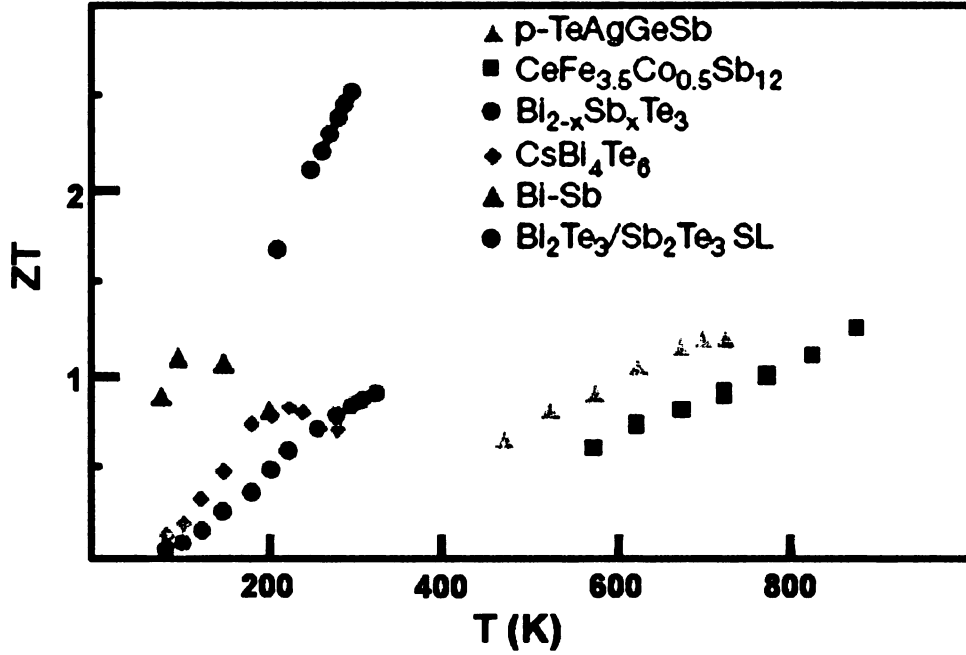


Figure 1.11:  $ZT$  value of 1 nm/5 nm p-type  $\text{Bi}_2\text{Te}_3/\text{Sb}_2\text{Te}_3$  superlattice as a function of temperature. Notice its conspicuous thermoelectric figure of merit compared to those of other materials. Adapted from [42].

Appropriately doped  $m = 18$   $n$ -type semiconducting sample exhibits a  $ZT$  value of  $\sim 2.2$  at 800 K [44]. It crystallizes in an average NaCl structure with Ag, Pb, and Sb atoms occupying the Na site and Te atoms the Cl site. However, high resolution transmission electron microscopy [45] and the atomic pair distribution function [46] studies revealed that the material is not a solid solution between  $\text{AgSbTe}_2$  and  $\text{PbTe}$  but Ag-Sb rich nanosized clusters ( $2 \sim 4$  nm in size) are randomly embedded in the  $\text{PbTe}$  matrix (Figure 1.12). These naturally occurring nano-clusters seem to be formed in order to reduce the Coulombic energy of the system: isoelectrically substituted  $\text{Ag}^+$  and  $\text{Sb}^{3+}$  ions tend to be close to each other for overall charge balance of the system segregating from  $\text{Pb}^{2+}$ -rich region [44]. Electronic structure calculations suggest that the microstructured Ag-Sb atoms may play an important role in its high power factor [47]. In addition to this, nanoscale clusters may also increase phonon scattering resulting in remarkable thermoelectric properties in  $\text{AgPb}_{18}\text{SbTe}_{20}$  [45, 46].

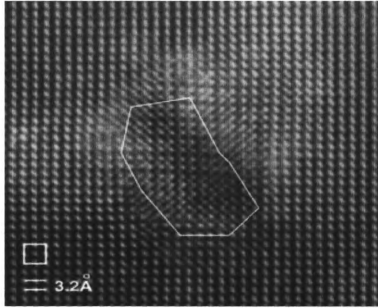


Figure 1.12: High resolution transmission electron microscopy image of Ag-Sb-rich nano-cluster embedded in the PbTe matrix in  $\text{AgPb}_{18}\text{SbTe}_{20}$  (region enclosed by white line). The typical cluster size is  $2 \sim 4$  nm. Adapted from [44].

While searching for  $p$ -type thermoelectric materials which are equally efficient to  $\text{AgPb}_{18}\text{SbTe}_{20}$ , Androulakis *et al.* studied the  $p$ -type  $\text{Ag}(\text{Pb}_{1-y}\text{Sn}_y)_m\text{SbTe}_{2+m}$  series [48]. The materials exhibit very low thermal conductivities which show no significant dependence on either the change in  $m$  and/or  $y$ , or the introduction of point defects. High-resolution transmission electron microscopy images revealed striking compositional fluctuations between Ag, Sb, and Pb/Sn with a length-scale of  $\sim 3$  nm and nanocrystals with  $5 \sim 20$  nm size in several samples of  $\text{Ag}(\text{Pb}_{1-y}\text{Sn}_y)_m\text{SbTe}_{2+m}$  (Figure 1.13). The exceptionally low thermal conductivity, and consequently high  $ZT$ , of  $\text{Ag}(\text{Pb}_{1-y}\text{Sn}_y)_m\text{SbTe}_{2+m}$  is most likely due to these nanometer-scale inhomogeneities.

One of the main reasons that nanostructured thermoelectric materials exhibit exceptionally high  $ZT$  values is their greatly reduced thermal conductivities which are much lower than those found in alloys. In alloys atomic substitutions scatter the short-wavelength acoustic phonons but the mid-to long-wavelength phonons stay

mostly unaffected conducting heat [40]. Do nanostructures really effectively scatter the mid- to long-wavelength phonons and lead to very low thermal conductivity? Kim *et al.* closely examined the changes in thermal conductivity of  $\text{In}_{0.53}\text{Ga}_{0.47}\text{As}$  when ErAs nanoparticles, of various sizes, were embedded [41]. They found that reduction in thermal conductivity of the sample with small size nanoparticles was not as significant as one with larger size verifying that the size of nano particles should be sufficiently large enough to scatter the mid- to long-wavelength phonon. In other words, point defects are not large enough to efficiently scatter such phonons. The largest reduction was found in the sample where  $1 \sim 4$  nm sized nanoparticles were randomly distributed. Compared to  $\text{In}_{0.53}\text{Ga}_{0.47}\text{As}$ , the thermal conductivity was reduced by almost a factor of 2 and the resulting  $ZT$  is increased more than a factor of 2. This study confirms that nanostructuring is an important component for high thermoelectric efficiency, especially to achieve very low thermal conductivity, in those extraordinary thermoelectric systems.



Figure 1.13: Compositional fluctuations between Ag, Sb, and Pb/Sn with a length-scale of  $\sim 3$  nm (wavy pattern) in  $\text{Ag}_{0.5}\text{Pb}_6\text{Sn}_2\text{Sb}_{0.2}\text{Te}_{10}$  captured by high-resolution transmission electron microscopy.  $ZT$  value of  $\sim 1.45$  was reported in this composition at 627 K. Adapted from [48].

## 1.4 Thesis layout

This thesis is organized as follows: The next chapter provides a brief introduction into the atomic pair distribution function (PDF) technique and x-ray and neutron powder diffraction experiments. The rapid acquisition pair distribution function technique for synchrotron x-ray based powder diffraction experiment is also discussed. Chapter 3 presents detailed local structural studies on  $\text{CeTe}_3$  to understand the true nature of incommensurate charge density wave in  $\text{CeTe}_3$  at 300 K. This is followed by the local structural studies on phonon-glass thermoelectric materials  $\beta\text{-Zn}_4\text{Sb}_3$  to search for the structural origin of its very low thermal conductivity. Finally, in Chapter 5 concluding remarks are accompanied with comments on possible future research avenues for the local structural studies of this class of novel charge density wave and thermoelectric materials, which concludes the thesis.



# Chapter 2

## The Atomic Pair Distribution Function Technique

### 2.1 The atomic Pair Distribution Function

Emerging functional materials often exhibit physical and structural complexity. Unusual properties of those materials are often closely related to their structural disorder [49, 50] or the information that we are interested in is usually the *local* atomic arrangement of such a system [3]. Therefore, techniques that probe local structure such as extended x-ray absorption fine structure (EXAFS) [51] or nuclear magnetic resonance (NMR) [52] are important tools to study these new materials. In this work we used the reduced atomic pair distribution function (PDF) technique, which is a local structural probe based on total scattering approach [49].

The pair distribution function is a one-dimensional interatomic distance distribution function which gives the probability of finding atom pairs separated by a distance  $r$  [49]. Figure 2.1 (a) depicts a model the two-dimensional square lattice with the lattice parameter of 2 Å. The corresponding pair distribution function (radial distribution function,  $R(r)$  in this case) is shown in the Figure 2.1 (b). The way to understand the PDF is as follows: first select an reference atom  $\nu$  (one indicated

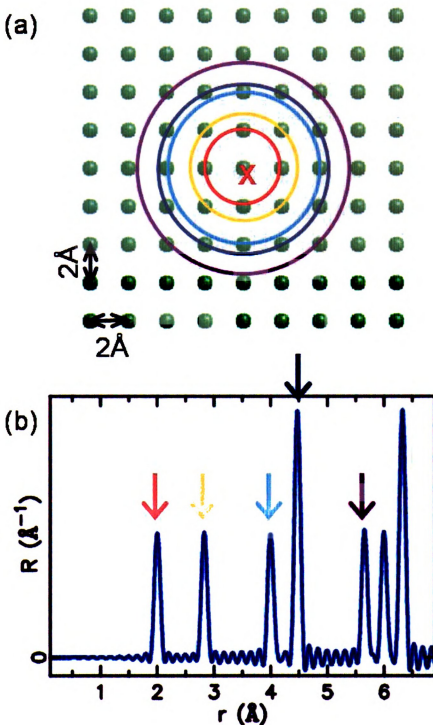


Figure 2.1: (a) A two-dimensional square lattice with lattice parameter of the  $2\text{\AA}$  and (b) the corresponding radial distribution function  $R(r)$ . The first peak in  $R(r)$  corresponds to correlations between the reference atom, which is crossed in red, and its nearest neighbor atoms, which coincide with the red circle in (a). The second peak is the second neighbor shell (yellow circle), and so on. This figure is in color.

by a cross in Figure 2.1 (a)), then gradually increase the radius of inspection from the reference atom, if atoms ( $\mu$ ) are found at a given radial distance  $r_{\nu\mu}$ , a peak appears in the distribution function at that distance. For example, the red circle in Figure 2.1 (a) coincides with the four first nearest neighbored atoms which are 2 Å apart from the reference atom and the corresponding peak appears at 2 Å in the pair distribution function. The same procedure is repeated for all the atoms in the system as a reference and then average is taken to obtain the distribution function. In the square lattice example, because there is no structural distortion or disorder, the pair distribution function obtained from a single reference atom is the same as the averaged one.

There are several forms of the pair distribution function. The atomic pair density function  $\rho(r)$  is given by

$$\rho(r) = \rho_0 g(r) = \frac{1}{4\pi N r^2} \sum_{\nu} \sum_{\mu} \delta(r - r_{\nu\mu}), \quad (2.1)$$

where  $\rho_0$  is the number density in the system of  $N$  atoms,  $\delta$  is a Dirac delta function.  $r_{\nu\mu} = |\mathbf{r}_{\nu} - \mathbf{r}_{\mu}|$  is the distance separating the  $\nu$ th and  $\mu$ th atoms. The function  $g(r)$  is called the atomic pair distribution function. It sums over all the atoms in the sample. The radial distribution function  $R(r)$ , that was used for the example above, is related to  $g(r)$  by

$$R(r) = 4\pi r^2 \rho_0 g(r). \quad (2.2)$$

The integrated area of the  $R(r)$  peak yields the corresponding coordination number, or number of neighbors at that distance. The reduced pair distribution function,  $G(r)$ , is one of widely used correlation functions. It is defined as

$$G(r) = 4\pi r \rho_0 (g(r) - 1). \quad (2.3)$$

The advantage of the reduced pair distribution function is that it is directly obtained from the Fourier transform of the total scattering structure function  $S(Q)$  which is measured quantity. For the sake of clarity, throughout this thesis the atomic pair distribution function (PDF) indicates the reduced pair distribution function  $G(r)$  unless it is specified.

## 2.2 PDF as a technique of choice

As mentioned earlier, it is of interest to understand the role of the local structural disorder or order which persists on a length scale less than 10 nm. Examples of such systems are structure of a nanostructured bulk materials where domains of local structural order exist over nanometer-length scales without destroying the average structure, the substructures of chemical species intercalated inside the pores of mesoporous materials, and the structures of nanoparticles [3]. Local structural probes such as NMR [52] and EXAFS [51] are often used to obtain the local structural information of these material. However, these methods are only feasible to explore local environments up to approximately 5 Å or less. Therefore, they do not provide intermediate range structural information. However, the PDF, which is another often used local structural probe, can provide further information as demonstrated in Figure 2.2.

## 2.3 Obtaining the experimental PDF

Similar to crystallography, the PDF makes use of scattering intensities from x-ray or neutron experiments. What we collect in a diffraction experiment is photon or neutron counts as a function of diffraction angle, or energy, or time of flight (please see Section 2.3.3) and so on, which will be converted to a  $Q$  value.  $Q$  is the magnitude of the diffraction vector or the momentum transfer  $\mathbf{Q}$  and for the elastic scattering

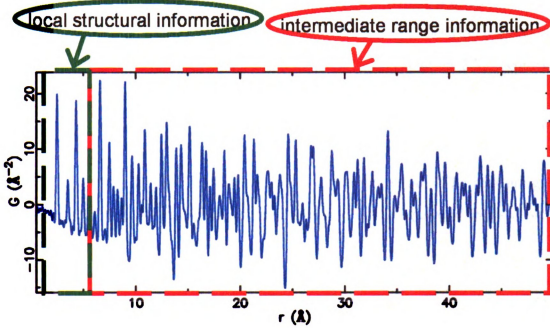


Figure 2.2: PDF provides both short and intermediate range order structural information.

case it is defined by

$$Q = |\mathbf{Q}| = |\mathbf{k}_i - \mathbf{k}_f| = \frac{4\pi \sin \theta}{\lambda}, \quad (2.4)$$

where  $\mathbf{k}_i$  is the wavevector of the incoming beam,  $\mathbf{k}_f$  is the wavevector of the scattered beam,  $\lambda = 2\pi/|\mathbf{k}_i| = 2\pi/|\mathbf{k}_f|$ , and  $\theta = 2\theta/2$  where  $2\theta$  is the angle between the incident and diffracted beams. A scattering event occurs when a particle interacts with a potential. X-rays and neutrons interact relatively weakly with atoms and the scattering amplitude for elastic scattering is given by

$$f_{\mathbf{k}_i, \mathbf{k}_f}(\theta, \phi) = \langle \int e^{i\mathbf{k}_i \cdot \mathbf{r}} U(\mathbf{r}) e^{-i\mathbf{k}_f \cdot \mathbf{r}} d^3r \rangle. \quad (2.5)$$

The brackets indicate a time average.  $U(\mathbf{r})$  is the scattering potential of the sample and thus can be written as a superposition of the potentials from each atom,

$$U(\mathbf{r}) = \sum_{\alpha=1}^N U_{\alpha}(\mathbf{R}_{\alpha}), \quad (2.6)$$

where  $N$  is the total number of scatterers and  $\mathbf{R}_\alpha = \mathbf{r} - \mathbf{r}_\alpha$ .  $\mathbf{r}$  and  $\mathbf{r}_\alpha$  denote the observation-point with respect to the origin and the scatterer ( $\alpha$ ) position with respect to the origin, respectively. Then the scattering amplitude (Equation 2.5) becomes

$$f_{\mathbf{k}_i, \mathbf{k}_f}(\theta, \phi) = \sum_{\alpha} U_{\alpha}(\mathbf{Q}) \langle e^{i\mathbf{Q} \cdot \mathbf{r}_{\alpha}} \rangle, \quad (2.7)$$

where  $U_{\alpha}(\mathbf{Q})$  is the Fourier transform of the atomic potential. The scattering intensity  $I(\mathbf{Q})$ , which is obtained from the experiment, is the square of this scattering amplitude. For the case of a sample with one type of atom,

$$I(\mathbf{Q}) = U^2(\mathbf{Q}) \langle \sum_{\alpha, \beta} e^{i\mathbf{Q} \cdot (\mathbf{r}_{\alpha} - \mathbf{r}_{\beta})} \rangle. \quad (2.8)$$

Thus the scattering intensity (Equation 2.8) is the product of the square of the atomic potentials  $U(\mathbf{Q})$  (the form factor) and a term which depends only on the arrangement of atoms, the structure function,

$$S(\mathbf{Q}) = \langle \sum_{\alpha, \beta} e^{i\mathbf{Q} \cdot (\mathbf{r}_{\alpha} - \mathbf{r}_{\beta})} \rangle. \quad (2.9)$$

It is convenient to normalize  $S(\mathbf{Q})$  by dividing by  $N$  ( $S^1(\mathbf{Q}) = S(\mathbf{Q})/N$ ) and define a coherent structure function as

$$S(\mathbf{Q}) = \frac{S^1(\mathbf{Q})}{\langle b \rangle^2} - \frac{\langle b^2 \rangle - \langle b \rangle^2}{\langle b \rangle^2}, \quad (2.10)$$

where the form factor in the case of neutrons  $U(\mathbf{Q})=b$  (scattering length) was used and  $\langle b \rangle$  represents a compositional average of the scattering length of the sample. For the case of the powder diffraction experiments, the scattering is isotropic and the directional information is lost. Now  $S(Q)$  is the normalized, measured, scattering intensity from a powder sample and it is called the total scattering structure function.

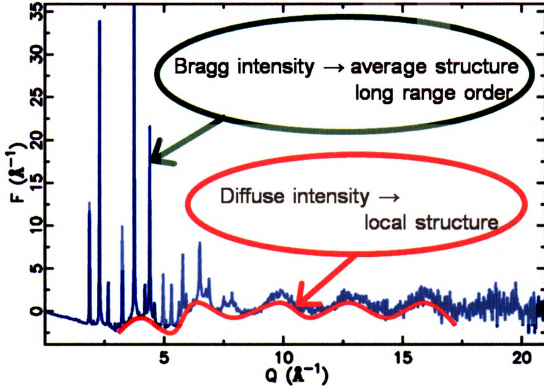


Figure 2.3: An example of the reduced total scattering structure function  $F(Q) = Q[S(Q) - 1]$ . Neutron powder diffraction data of  $\text{Ag}_2\text{O}$ , which shows a huge negative thermal expansion effect, were collected at 300K. There are two pronounced features in this  $F(Q)$ ; Bragg intensities which give the average structural information and diffuse intensities that provide the local deviations from the average structure.

Finally we obtained the PDF by Fourier transformation of  $F(Q) = Q[S(Q) - 1]$ ,

$$G(r) = \frac{2}{\pi} \int_0^\infty Q[S(Q) - 1] \sin Qr dQ. \quad (2.11)$$

An example of  $F(Q)$  from neutron powder diffraction data is shown in Figure 2.3. It contains two types of features: sharp well defined peaks (Bragg intensities) and diffuse background under or between the Bragg peaks (diffuse intensities). In crystallography, only Bragg intensities and positions are treated to determine the average structure and diffuse intensities are discarded as a background. However, completely ignoring diffuse scattering is throwing away valuable structural information, since diffuse scattering arises from any temporary or permanent breakdown of space group

symmetry [53]. Therefore, it provides information about the local structural deviations, especially deviations that are locally correlated, from the average structure [49]. As it is seen from Equation 2.11, the PDF is obtained by sine Fourier transform of the entire  $F(Q)$ , hence it treats both Bragg and diffuse scattering intensities eventually. For this reason, the PDF is called the total scattering technique [49].

The diffuse scattering in powder diffraction data is almost  $Q$ -independent (Figure 2.3); at low- $Q$  region diffuse scattering lies underneath the Bragg peaks and it remains and becomes significant at high- $Q$  region where Bragg peaks are diminished due to the Debye-Waller factor which reflects the effect of atomic motion due to thermal or zero-point quantum vibrations. For the PDF analysis, it is important to have signal at high  $Q$  ( $Q \geq 25 \text{ \AA}^{-1}$ ) with good statistics, since it determines the real space resolution in the PDF. The higher the  $Q_{max}$  used, the better two closely placed PDF peaks would be resolved. Therefore, the advent of synchrotron based x-ray and spallation neutron sources, that generate high energy, flux beams, made it possible to measure highly accurate PDFs [49].

### 2.3.1 X-ray powder diffraction

#### Production of x-rays

Most commonly used radiation source for powder diffraction measurements is x-ray. Typical wavelengths of the x-rays range from  $\sim 0.1$  to  $\sim 100 \text{ \AA}$  [2]. Most of the time the x-rays available in a laboratory are generated in an x-ray tube. The tube is usually made of glass and an anode and cathode are placed inside of the vacuumed glass tube. Electrons are emitted from the electrically heated tungsten filament cathode and an electrostatic potential (30 to 60 kV) applied between the cathode and the anode accelerates those electrons towards the anode. The typical current is  $10 \sim 50 \text{ mA}$  [2]. The high-energy electrons bombard a metal target (such as copper, molybdenum, or silver) knocking out electrons from inner shells of atoms in the metal target. The



Table 2.1: X-ray energies ( $K\alpha_1$  emission energies), wavelengths, and  $Q_{max}$  values for laboratory x-ray sources. The  $Q_{max}$  values are calculated with a maximum accessible scattering angle of  $160^\circ$ .  $\beta$ -filter elements for each source are also listed. Adapted from [49].

Source	$E_0$ (keV)	$\lambda$ (Å)	$Q_{max}$ (Å $^{-1}$ )	$\beta$ -filter element
Cu	8.05	1.538	8.0	Ni
Mo	17.48	0.708	17.5	Nb, Zr
Ag	22.16	0.559	22.0	Rh

x-rays are produced when outer shell electrons drop down filling those empty states. Characteristic lines found in a typical x-ray emission spectrum are  $K\alpha$  (L shell  $\rightarrow$  K shell) and  $K\beta$  (M shell  $\rightarrow$  K shell). Characteristics of commonly used laboratory x-ray sources are summarized in Table 2.1.

High flux and high energy synchrotron x-rays are favorable for the PDF studies. In synchrotron rings electrons or positrons are moving in a circular orbit through magnetic fields at relativistic velocities. The x-rays are produced due to the acceleration of electrons or positrons towards the center of the ring [2] and emitted in the tangential direction to the charged particle orbit. Quite a wide energy range of x-rays up to the MeV range are produced with high intensities allowing to select nearly any desired wavelength very easily.

## Collimation and Monochromatization

The process of selecting electromagnetic waves with parallel or nearly parallel propagation vectors (collimation) is required to reduce angular divergence (dispersion) of the primary x-ray beam. The angular divergence often leads to broad and asymmetric Bragg peaks [2]. Collimation can be achieved by placing a slit between the x-ray source and the sample. The dimensions of the source, the size, and the placement of

the slit determines the angular divergence of collimated beam. Additional collimation can be achieved by placing another slit further on the way of the beam.

Monochromatization, the process to convert polychromatic radiation into a single wavelength, is necessary to avoid a high background due to white radiation and multiple Bragg peaks from each set of crystallographic planes. The way to eliminate  $K\beta$  radiation from laboratory x-ray is placing a filter that can absorb  $K\beta$  radiation. The  $\beta$ -filter makes use of the x-ray absorption properties of chemical elements. When x-rays travel through the matter, they are partially transmitted and partially absorbed. The absorption will be maximized if the x-ray energy (wavelength  $\lambda$ ) match to excitation energy of K electrons of the atoms in the matter. In general the  $\beta$ -filter is made of a material whose element has one atomic number less than the anode material in the periodic table. The most commonly used  $\beta$ -filter elements for laboratory x-ray sources are listed in Table 2.1. Disadvantages of  $\beta$ -filters are that they do not eliminate  $K\beta$  intensity completely, thus leave a considerable amount of white radiation after filtering, and also they reduce the intensity of  $K\alpha$  line.

More complex but much improved way of monochromatizing x-rays is use of single crystal monochromators. It takes advantage of diffraction from a high-quality single crystal. The x-rays in divergent beam reach the monochromator with slightly different incident angles ( $\theta_1 \leq \theta \leq \theta_2$ ). They are reflected at the crystal surface according to Bragg's law;

$$2d \sin \theta = n\lambda \quad (2.12)$$

where  $d$  is the interplanar distance of the crystal,  $\theta$  is the incident angle and  $\lambda$  is the wavelength. Therefore, of the x-rays with an incident angle  $\theta_1$  ( $\theta_2$ ) only a particular wavelength  $\lambda_1$  ( $\lambda_2$ ) is diffracted with the angle  $\theta_1$  ( $\theta_2$ ). Shorter wavelength x-rays fall into the low Bragg angle range and longer wavelengths are found at the high Bragg angles. Monochromatic beam in a desired range can be easily selected by a slit properly placed in the path of x-rays reflected by a crystal monochromator and

the wavelength resolution can be improved by using diffraction from two or more monochromators in a sequence. Commonly used crystal monochromators are made of pyrolytic graphite, Si, Ge, or LiCl [2]. Both collimation and monochromatization should be done with the minimal loss of intensity.

### **Detection of x-rays**

The detection is based on the ability of x-rays to interact with matter and to produce certain effects or signals, for example to generate particles, waves, electrical current, etc., which can be easily registered. Detectors can be classified as point detectors and line or area detectors depending on whether the detector is capable of resolving the location where the photon has been absorbed in addition to counting the number of photons. A point detector, such as gas proportional counter, scintillation and solid-state detectors, registers only the intensity of the diffracted beam, one point at a time. Thus, to examine the distribution of the diffracted intensity as a function of Bragg angle using a point detector, it is necessary to perform multiple point measurements at varying Bragg angles. Line or area detectors support spatial resolution. They are similar to photographic film whose entire area is exposed simultaneously. Three types of line and area detectors are commonly used in powder diffraction experiments: position sensitive (PSD), charge coupled devices (CCD), and image plates (IPD). The former is a line detector and the latter two are area detectors. Both line and area detectors can measure diffracted intensity at multiple points at once and thus, a single measurement results in the diffraction pattern resolved in one or two dimensions, respectively. All of the X-ray powder diffraction experiments for this thesis are carried out using an image plate detector. Detailed experiment setup is described in the following section.

### 2.3.2 Rapid Acquisition Pair Distribution Function (RAPDF) technique

As the atomic scale structural information becomes essential to understand interesting properties of emerging functional materials, demand on powder diffraction data that are feasible for the PDF analysis hugely increases. Studies on nano-crystalline and crystalline materials often require high real-space resolution PDFs (high  $Q_{max}$  value) and point detectors are usually used in the conventional PDF measurements. Since data are collected over wide angular ranges and good statistics at high  $Q$  regions are essential for the PDF analysis, each measurement requires generally at least eight hours of data collection times for conventional experimental setup, even with synchrotron x-rays [54]. This extremely slow data collection process was overcome by combining synchrotron radiation with a two-dimensional image plate detector. This is so called the rapid acquisition pair distribution function (RAPDF) technique, which greatly reduces the data collection time by three to four orders of magnitude [54]. The typical RAPDF setup is illustrated in Figure 2.4. The heart of the RAPDF technique is making use of an area detector that can measure the entire scattering range simultaneously and can readout collected information rapidly. A Mar345 image plate detector, a round disk with usable diameter of 345 mm is often used. The RAPDF technique also makes it possible to do parametric PDF studies with very dense data points [55].

### 2.3.3 Neutron powder diffraction

Beams of neutrons are often used as a probe in PDF experiments. From quantum mechanics, neutrons behave as waves with de Broglie wavelength  $\lambda$ :

$$\lambda = \frac{h}{mv} \quad (2.13)$$

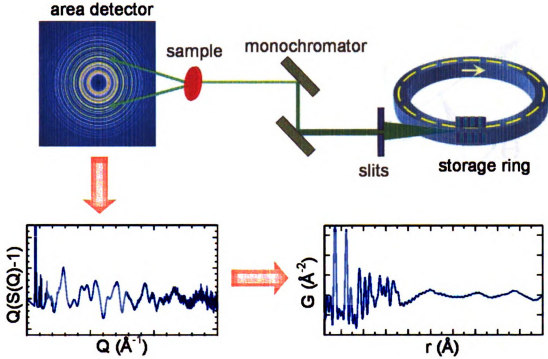


Figure 2.4: The RAPDF experimental setup. It utilizes a two-dimensional image plate detector with synchrotron radiation source that overcomes the issue of long data collection time of the conventional method [54]. The image plate is mounted orthogonally to the beam path with the beam centered on the image plate.

where  $h$  is Planck's constant ( $h=6.626 \times 10^{-34}$  J.s),  $m$  is the neutron's rest mass ( $m=1.6749 \times 10^{-27}$  kg), and  $v$  is the neutron's velocity. For example, a neutron moving with a constant velocity  $v = 3000$  m/s will also behave as a wave with  $\lambda=1.319$  Å.

Pulsed neutrons can be produced by a spallation method. In this method high energy protons ( $\sim 1$  GeV) bombard a target of a heavy metal such as tungsten or uranium and neutrons from the nuclei of the target element are knocked out. These neutrons are fast with the energy of several MeV and slowed down by a moderator which is usually made of water or organic solid or liquid methane [49]. This process yields neutron pulses with an energy spectrum in the thermal and epithermal ranges. The shape of the neutron spectrum is characterized by measuring vanadium which

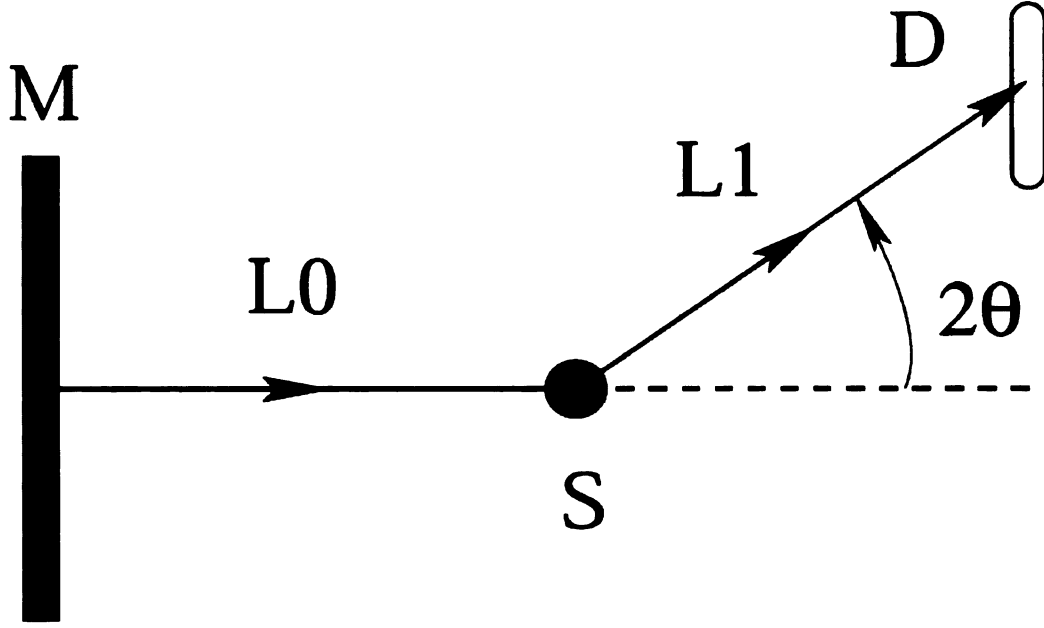


Figure 2.5: Geometry of the time-of-flight experiment setup. M, S, and D indicate a moderator, powder sample, and detector, respectively.  $L_0$  is the length of the path that neutrons travel from the moderator to the sample and  $L_1$  is that of scattered neutrons flight from the sample to the detector. Credit: E. S. Božin.

scatters neutrons incoherently. Scattering data using these pulsed neutrons are collected using the time-of-flight (TOF) method. The neutrons having different energies (wavelengths) have different velocities. Therefore, neutrons in a pulse arrive at the sample (S in Figure 2.5) at different times and scattered neutrons with different wavelengths also reach a detector (D in Figure 2.5) at different times. In this method, a detector fixed at a certain angle  $2\theta$  with respect to the incident beam (Figure 2.5) can provide a complete powder diffraction intensity profile (intensity vs  $Q$ ) since  $\lambda$  is varying in Bragg's law (Equation 2.12) for this setup. If the total traveling length of the neutrons leaving the moderator is  $L = L_0 + L_1$ , using Equation 2.4 the magnitude of the diffraction vector  $Q$  can be obtained by the equation,

$$|Q| = Q = \frac{2m_N L}{\hbar t} \sin \theta \quad (2.14)$$

where  $t$  is the time of flight over the path  $L$  and  $m_N$  is the neutron mass. In

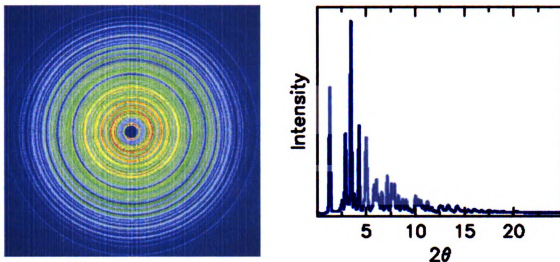


Figure 2.6: A two-dimensional image dataset from the RAPDF experiment (left). The dataset is converted to intensity vs  $2\theta$  format (right).

principle a single detector can be used for the experiment but filling more solid angle with detectors greatly increases efficiency of the data collection.

## 2.4 Data processing, analysis, and modeling

### 2.4.1 RAPDF data processing

An example of two-dimensional image data obtained from the RAPDF experiment is shown in Figure 2.6. Silicon is routinely measured to obtain calibration parameters such as the sample to detector distance. Several datasets were combined, averaged, and converted to intensity versus  $2\theta$  format using the Fit2D program [56], where  $2\theta$  is the angle between the incident and diffracted x-rays. Signal from an empty container is also measured as a background. The measured background is subtracted from the data and standard corrections such as multiple scattering, polarization, absorption, Compton scattering, and Laue diffuse scattering are applied [49] using the PDFgetX2 program [57]. The corrected dataset is further processed to obtain the reduced total scattering structure function  $F(Q)$  and finally  $F(Q)$  is sine Fourier transformed to

get the atomic pair distribution function  $G(r)$ .

### 2.4.2 Neutron data processing

In order to take the length of the measurement and the fluctuations in neutron spectrum into account each data set is normalized by the total integrated intensity. Backgrounds from a vanadium sample container and the sample environment are measured and subtracted. Standard corrections such as multiple scattering, absorption, incoherent and inelastic scattering are made [49] and then the corrected intensities are divided by the intensity of vanadium standard to correct for the incident spectrum. The reduced total scattering structure function  $F(Q)$  is obtained from properly normalized corrected intensities and the PDF,  $G(r)$ , is obtained via Fourier transform of  $F(Q)$ . This procedure is done using the program PDFgetN [58].

### 2.4.3 Structural modeling

Structural information is extracted from the experimental PDF performing a full profile real space refinement [59]. The least square method based program PDFFIT2 [60] and PDFgui [61] are used for structural modeling. Initial values for structural parameters such as space group, lattice parameters, fractional atomic coordinates are obtained from literature or Rietveld refinement on Bragg intensities. Then those parameters are refined until the model provides the best agreement to the data *i.e.* the difference between the calculated and the experimental PDFs becomes minimal for a given refinement range. The model PDF is calculated according to the equation

$$G_{calc}(r) = \frac{R(r)}{r} - 4\pi r \rho_0, \quad (2.15)$$



where

$$R(r) = \frac{1}{N} \sum_{\nu} \sum_{\mu} \frac{b_{\nu} b_{\mu}}{\langle b \rangle^2} \delta(r - r_{\nu\mu}), \quad (2.16)$$

$b_i$  is the scattering length of the  $i$ th atom, and  $\langle b \rangle$  is the average scattering power of the sample. The sum goes over all the pairs of atoms in the sample [59]. Each contribution given by  $\delta(r - r_{\nu\mu})$  is convoluted with a Gaussian accounting for the displacements [60]. The goodness of fit is indicated by the weighted agreement factor

$$R_w = \sqrt{\frac{\sum_{i=1}^N \omega(r_i) [G_{obs}(r_i) - G_{calc}(r_i)]^2}{\sum_{i=1}^N \omega(r_i) G_{obs}^2(r_i)}}, \quad (2.17)$$

where  $G_{obs}$  and  $G_{calc}$  are the observed and calculated PDFs and  $\omega$  is the weighting factor,  $\omega(r_i) = 1/\sigma^2(r_i)$ , where  $\sigma$  is the estimated standard deviation on the  $i$ th data-point at position  $r_i$  [49]. The refinement result on the 300 K neutron nickel PDF is shown in Figure 2.7 and refinement parameters are summarized in the Table 2.2.

The initial structure was taken from the literature and space group  $Fm\bar{3}m$  was kept during the refinement. The refinement range was  $1.5 < r < 10$  Å. The final  $R_w$  value is small and the refined value of the isotropic displacement parameter ( $U_{iso}$ ) is reasonable for 300 K data. These indicate that the average and local structures of Ni

Table 2.2: Refined structural parameters for Ni. The neutron PDF was obtained at 300 K.  $Q_{max}$  of  $27 \text{ Å}^{-1}$  was used and the refinement range was  $1.5 < r < 10$  Å.

	initial values	refined values
$a$ (Å)	3.52	3.5296(5)
$U_{iso}$ (Å <sup>2</sup> )	0.0086	0.0045(1)
$R_w$	N/A	0.05531

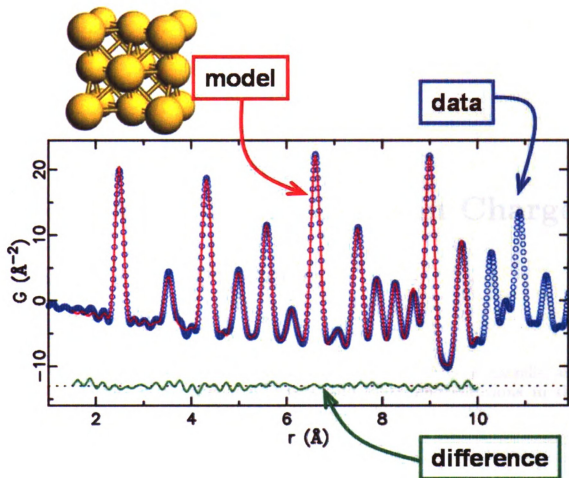


Figure 2.7: Structural modeling on the experimental neutron Ni PDF obtained at 300 K. Blue open circle and red line represent the experimental and calculated PDFs, respectively. The difference between two PDFs is plotted below them (green line). This figure is in color.

agree.

# Chapter 3

## Local structure of $\text{CeTe}_3$ in Charge Density Wave state

H. J. Kim, C. D. Malliakas, A. T. Tomić, S. H. Tessmer, M. G. Kanatzidis, and S. J. L. Billinge, **Local atomic structure and discommensurations in the charge density wave of  $\text{CeTe}_3$** , Phys. Rev. Lett. **96**, 226401 (2006).

### 3.1 Introduction

Incommensurate charge density waves (IC-CDWs) are a fundamental property of low-dimensional metals [4] and also underly the novel properties of correlated electron oxides such as cuprates in the pseudo-gap state [62, 63, 64], and manganites at high doping [65]. Knowing the nature of local atomic displacements (Peierls distortions) in the IC-CDWs is crucial to understand such factors as electron-lattice coupling [66], yet this information is difficult to obtain quantitatively. Here we solve this problem by taking the novel approach of using a local structural method, the atomic pair distribution function (PDF) technique [49], to determine the local atomic displacements with high precision in the system  $\text{CeTe}_3$ . IC-CDWs, and the underlying atomic displacements, can be uniform incommensurate modulations or locally commensurate waves separated by narrow domain walls, known as discommensurations [7], where

the phase of the wave changes rapidly. Here we show that the IC-CDW in  $\text{CeTe}_3$  is discommensurated and obtain for the first time the quantitative local atomic displacements within the commensurate domains.

### 3.1.1 Discommensurations in IC-CDW

In the case of *incommensurate* CDWs, superlattice peaks observed crystallographically yield the average distorted structure. Except in the cases where the domains are periodically arranged, giving rise to satellite peaks [67], it is not possible to determine whether the underlying CDW is truly incommensurate or forms a discommensurated structure with commensurate regions separated by domain walls [7]. A number of techniques have been successful at differentiating between the truly incommensurate and discommensurated cases. The earliest verification of a discommensurated phase came from photoemission spectroscopy evidence that the Ta  $4f$  states in  $1T\text{-TaS}_2$  had the same splitting in the commensurate and nearly-commensurate states [68]. Photoemission is a local probe and found distinct Ta environments rather than a broad continuum expected from a purely incommensurate state. Similarly, another local probe, nuclear magnetic resonance (NMR), found distinct Knight-shifts for three Se sites in the incommensurate state of  $2H\text{-TaSe}_2$ , similar to the commensurate phase [69, 70]. High resolution atomic imaging methods have also contributed to this debate. The strain fields due to the domain walls were observed in dark field transmission electron microscopy (TEM) measurements [71]. Interestingly, atomic resolution images in real-space have difficulty in resolving discommensurated domains [72, 73, 74, 75]. However, Fourier analysis of scanning tunneling microscopy (STM) images can be a reliable measure, as discussed in detail by Thomson *et al.* [76].

As in the case of the NMR and photoemission studies, the PDF approach described here makes use of the fact that the local structure deviates from the average in the discommensurated case. By comparing atomic displacements determined from

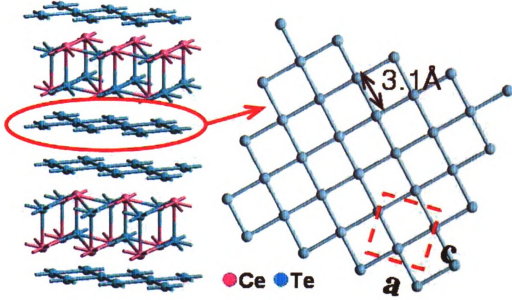


Figure 3.1: The crystal structure of  $\text{CeTe}_3$  with the square Te net where the charge density wave occurs. The reduced unit cell on the Te net is indicated by the red dashed box. This figure is in color.

the PDF with those determined crystallographically we establish the presence of commensurate domains, but crucially, also obtain quantitatively the atomic structure within these domains. This novel approach is here applied to the incommensurate phase of  $\text{CeTe}_3$ .

### 3.1.2 Average structure and CDW state of $\text{CeTe}_3$

In its undistorted form,  $\text{CeTe}_3$  takes the  $\text{NdTe}_3$  structure type with space group  $Cmcm$  [77]. It forms a layered structure with ionic  $[\text{Ce}_2^{3+}\text{Te}_2^{2-}]^{2+}$  layers sandwiched between two  $\text{Te}^-$  layers (Figure 3.1). These sandwich layers stack together with weak van der Waals forces to form the 3-dimensional structure. Te ions in the  $\text{Te}^-$  layers form a square-net with 3.1 Å Te-Te bonds. These Te-Te bonds are too long to be considered normal bonds and the true underlying structure of  $\text{CeTe}_3$  seems not to be unraveled completely with  $Cmcm$  structure. The electronic bands crossing the Fermi level are Te  $p$ -bands from the 2D square nets [78] and the CDW

forms in these metallic layers. In the CDW state an incommensurate superlattice is observed [78, 79], with a wavevector characteristic of a strong Fermi-surface nesting vector in the electronic structure [80, 81, 82, 83].

This is a surprisingly stable and simple single- $q$  IC-CDW state in an easily cleavable 2D square net making the  $\text{RETe}_3$  (RE=Rare Earth) systems ideal for studying the IC-CDW state [78]. The atomic distortions giving rise to the superlattice have been solved crystallographically from single crystal x-ray diffraction data [79]. The incommensurate wavelength of the distortion is close to  $25a/7$ , where  $a$  is the lattice parameter of the undistorted phase. The distorted structure is in the  $Ama2$  space-group [79]. From the crystallography alone it is not possible to determine whether this distorted structure is truly incommensurate or whether discommensurations form between short-range commensurate domains.

## 3.2 Experimental details

The X-ray PDF experiment was conducted on a fine powder of  $\text{CeTe}_3$  prepared as described in Ref. [79].  $\text{CeTe}_3$  powder was loosely packed in a flat plate with thickness of 1.0 mm sealed with kapton tape. Care must be taken when grinding this material or turbostratic disorder is introduced, significantly modifying the stacking of the layers.

Powder diffraction data were collected at 300 K at the 6-IDD station of MUCAT at the Advanced Photon Source (APS) at Argonne National Laboratory. The X-ray energy used was 130.001 keV ( $\lambda=0.0953715$  Å). Data were collected in rapid acquisition pair distribution function (RA-PDF) mode [54] using a circular image plate (IP) camera Mar345, 345 mm in diameter. The camera was mounted orthogonally to the beam path with a sample-to-detector distance of 217.685 mm which was determined by calibrating with a silicon standard sample [54].

In order to avoid saturating the detector, measurements were made for between 150 and 200 seconds, repeated three times to improve counting statistics. An example

of the raw data on the image plate is shown in Figure 3.2. The data were combined and integrated using the program FIT2D [84]. Various corrections were made to the data using the program PDFgetX2 [57], such as subtraction of background and container, Compton and fluorescence scattering, geometric corrections, absorption, and so on, as described in reference [49]. The properly normalized total scattering function,  $S(Q)$ , [49] was obtained and truncated at  $Q_{max}$  of  $25 \text{ \AA}^{-1}$  before Fourier transforming to obtain the PDF,  $G(r) = \frac{2}{\pi} \int_0^\infty Q[S(Q)-1] \sin(Qr) dQ$ . The structural modeling was carried out using the program PDFFIT2 [60].

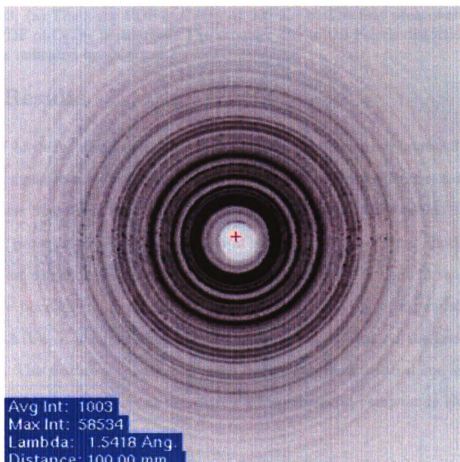


Figure 3.2: Raw Image plate data of CeTe<sub>3</sub> at 300 K.

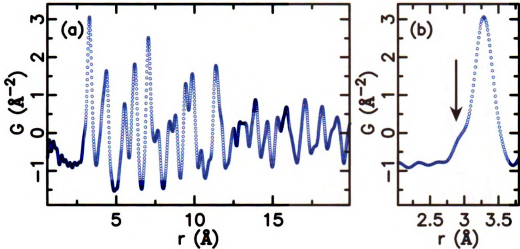


Figure 3.3: (a) The x-ray PDF of CeTe<sub>3</sub> at 300 K. (b) The first peak of the experimental PDF of CeTe<sub>3</sub> is enlarged. The shoulder due to the Peierls distortions in the Te nets is indicated by an arrow.

### 3.3 Results

The PDF of CeTe<sub>3</sub>, measured at room temperature, is shown in Figure 3.3 (a). The excellent signal to noise ratio of the data is evident from the negligibly small ripples on the base line of the PDF below 2.5 Å compared to the PDF peaks. The PDF gives the probability of finding an atom at a distance- $r$  away from another atom. The nearest neighbor peak around 3.1 Å comes from the Te-Te bond in the nets and the Ce-Te bond in the intergrowth layers. This is shown on an expanded scale in Figure 3.3 (b). A shoulder, indicated by an arrow, is evident on the low- $r$  side of the peak. This feature is robust; it is much larger than the statistical and systematic errors and is reproduced in measurements of isostructural compounds NdTe<sub>3</sub> and PrTe<sub>3</sub>.

Figure 3.4 (a) shows the fit to this peak of the undistorted crystal structure model (*Cmcm*), where only symmetry allowed atomic positions and isotropic thermal factors were refined. The result clearly does not explain this shoulder which originates from short Te-Te bonds in the Te-net. Surprisingly however, the PDF calculated from the *distorted* structure determined crystallographically [79] also does not ex-



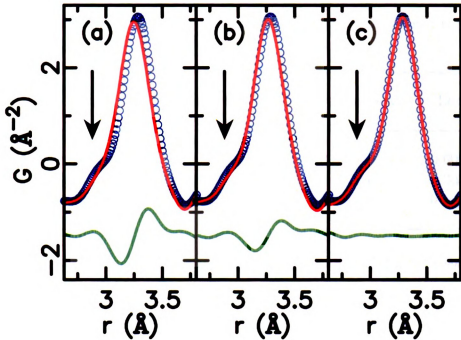


Figure 3.4: The first peak of the experimental PDF of  $\text{CeTe}_3$  (blue circles) is plotted with the calculated PDF (red line) from various models: (a) the undistorted crystal structure model ( $Cmcm$ ), (b) the distorted-crystallographic model, and (c) the local structural model determined from a PDF refinement over the range  $2.5 < r < 6.37 \text{ \AA}$ . The difference between the experimental and calculated PDFs is plotted below the data in each panel (green line). The shoulder due to the Peierls distortions in the Te-nets is indicated by an arrow. This figure is in color.

plain this shoulder well. In this case the atoms were fixed at the crystallographically determined positions and isotropic atomic displacement parameters ( $U_{iso}$ ) were refined. This resulted in a better fit to the first peak (Fig. 3.4 (b)); however, the fit is not ideal and required a large value of  $U_{iso}$  for the Te atoms in the nets ( $U_{iso} = 0.0152(2) \text{ \AA}^2$ ). The value was two times larger than  $U_{iso}$  of the Ce and Te atoms in the ionic  $[\text{Ce}_2^{3+}\text{Te}_2^{2-}]_{2+}$  layers ( $0.0077(2) \text{ \AA}^2$  and  $0.0080(2) \text{ \AA}^2$  for  $U_{iso}$  of Ce and Te atoms, respectively).  $U_{iso}$  values from the PDF refinements using three structural models are summarized in Table 3.1.

The large fluctuation in the difference curve in Figure 3.4 (a) arises because the real distribution of Te-Te bond-lengths in the data is broader than in the undistorted model. This fluctuation in the difference curve is smaller in Figure 3.4 (b) because the

Table 3.1: Isotropic atomic displacement parameters ( $U_{iso}$ ) from refined three structural models.  $U_{iso}$  is in the unit of  $\text{\AA}^2$ .

	Undistorted	Distorted-crystall.	Local
Ce	0.00821	0.00769	0.00691
Te in $[\text{Ce}_2^{3+}\text{Te}_2^{2-}]_{2+}$ layers	0.00671	0.00804	0.00685
Te in Te-nets	0.01869	0.01523	0.00692

distortions of the Te net in the *Ama2* crystallographic model result in a broader Te-Te bond-length distribution. However, clearly the distorted-crystallographic model still has a Te-Te bond-length distribution that is narrower than in the data. We therefore refined the Te-net distortions directly in the PDF by allowing the atomic positions in the model to vary. The model was constrained to have the *Ama2* symmetry and the same unit cell was used as in the distorted crystallographic model. The refinement result for  $2.5 < r < 6.37 \text{ \AA}$  is shown in Figure 3.4 (c). As well as giving a significantly better fit to the low- $r$  region of the PDF, this refinement resulted in much smaller and more physical thermal factors on the planar Te ions (Table 3.1).

### 3.4 Discussion

The model of the local structure refined from the PDF gives a broader range of Te-Te bond lengths (from  $2.83 \text{ \AA}$  to  $3.36 \text{ \AA}$ ) than the crystallographic distorted model (from  $2.94 \text{ \AA}$  to  $3.26 \text{ \AA}$ ). It is also interesting to see the shape of the bond-length *distributions* for the Te-Te bonds in the Te-nets from these two models. These are shown in Figure 3.5. The blue solid line shows the bond-length distribution refined from the PDF and the red line is the distribution from the crystallographic model [79]. For direct comparison the distributions are plotted using the same thermal broadening of  $0.007 \text{ \AA}^2$ . The distorted-crystallographic model has broad, but symmetric and

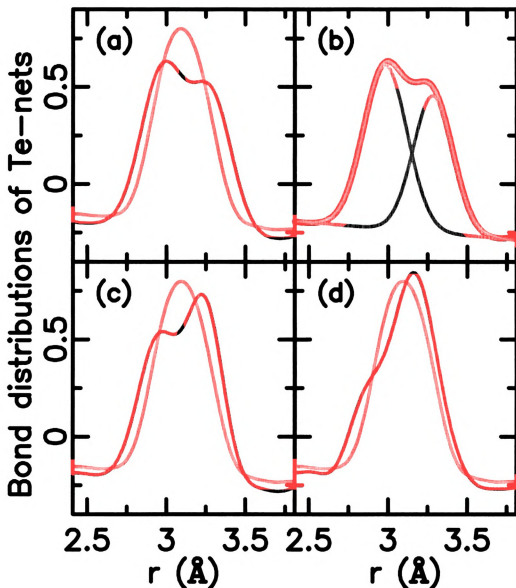


Figure 3.5: Bond-length distributions in the Te-nets refined from the PDF over various  $r$ -ranges (blue line) (a)  $r_{max}=6.37$  Å (b)  $r_{max}=6.37$  Å (c)  $r_{max}=14.5$  Å (d)  $r_{max}=27.1$  Å. The  $r_{min}$  value was fixed to 2.5 Å for all the cases. The bond distribution from the distorted crystallographic model (red line) is plotted in (a), (c), and (d) for comparison. In (b) the bond distribution of the local structural model ( $r_{max}=6.37$  Å) is fit with two Gaussians. The fit is shown as a red line and the two Gaussian sub-components in green lines. This figure is in color.



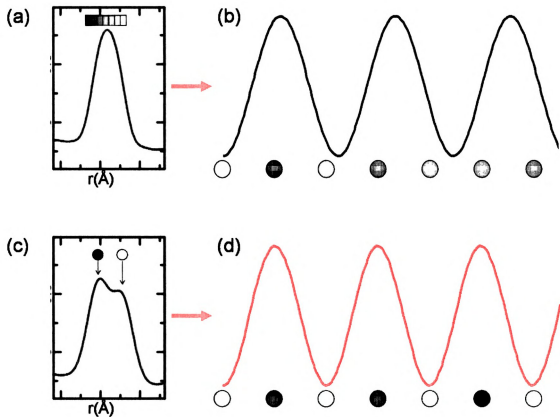


Figure 3.6: (a) Gaussian like bond-length distribution is found in (b) uniform incommensurate charge density waves whereas (c) bimodal bond-length distribution is found in (d) commensurate charge density waves. The circles indicate the position of bonds in the underlying lattice and the sinusoidal waves represent the spatial distribution of conduction electron charge density. The color of the circles indicates the length of the bond; shorter bonds in dark colors and longer bonds in light colors. In the case of the uniform IC-CDW the phase of the CDW with respect to the lattice, which modulates the bond-length, varies continuously giving rise to a broad distribution of bond-lengths. In C-CDW the wave is in-phase with the lattice yielding a limited number of bond-lengths. This figure is in color.

Gaussian bond-length distribution coming from the continuous distribution of Te-Te bond lengths in the *average* IC-CDW (Figure 3.6 (a-b)). On the other hand, the local structure refinement ( $r_{max} = 6.37 \text{ \AA}$ ) yields a bond-length distribution that is clearly bimodal and is separated into distinct “short” and “long” Te-Te distances. This is emphasized in Figure 3.5 (b) where we show a fit of two, well separated, Gaussian

curves to the PDF-refined bond-length distribution. This behavior is characteristic of oligomerization with Te forming bonded and non-bonded interactions with its neighbors in the net [85] that would be expected in a commensurate structure (Figure 3.6 (c-d)). Since we know that the modulation is incommensurate on average, this is strong evidence that the structure consists of commensurate domains separated by discommensurations. As  $r_{max}$  in the PDF-refinements is increased the PDF refined distribution crosses over towards the crystallographic result and by  $r_{max} = 27.1 \text{ \AA}$ , resembles it rather closely (Figure 3.5 (d)).

We have applied STM on the exposed Te net of a cleaved single crystal of  $\text{CeTe}_3$ , grown according to the method described in Ref. [79]. Measurements were done at 300 K in the constant current mode of the STM. Data were acquired with a bias voltage of 100 mV and with a tunneling current of 0.6 nA. Figure 3.7 (a) shows a representative atomic resolution image with the CDW modulation clearly visible oriented at  $45^\circ$  to the net. To investigate the images for discommensurations, we examine the corresponding two-dimensional Fourier transform, shown in Figure 3.7 (b). As indicated by the labels, in addition to the fundamental CDW peak (1), four more peaks lie along the CDW direction (2-5). Although the transforms of real space images resemble diffraction data, symmetry requirements intrinsic to diffraction data do not apply. As demonstrated by Thomson and co-workers, the Fourier transforms of STM images that exhibit true discommensurations always have extra peaks in proximity to the fundamental CDW peak [76]. This arises from the fact that a discommensurate CDW can be expressed as the product of a uniformly incommensurate CDW and a modulation envelope [76]. The wavelengths of the envelope are given by the differences in the wave vectors of closely spaced peaks. The longest such wavelength in our images is  $38 \text{ \AA}$ , corresponding to peaks 2-3 and 3-4 in the Fourier transform, indicating that a discommensuration separation of this length-scale exists. This is consistent with the refined PDF behavior which crosses over from the local to the

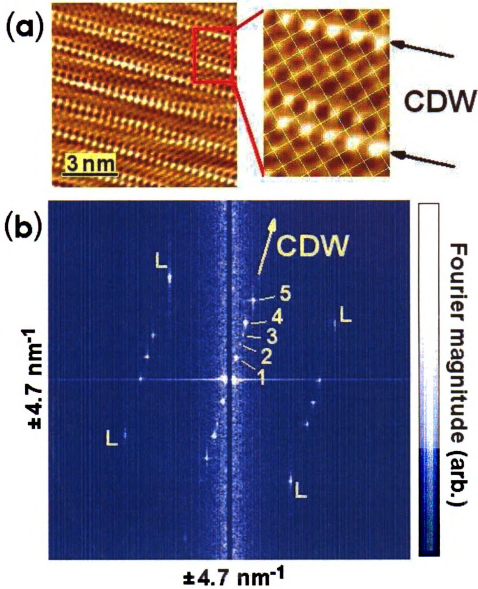


Figure 3.7: (a) A representative STM image from the Te net showing the CDW. On the expanded image, the network of Te bonds is superimposed. (b) The Fourier transform of the STM data. To achieve a high signal-to-noise ratio, the transform represents the average of 24 images (each image was  $27 \times 27 \text{ nm}$ ). The unprocessed transform image shows enhanced noise along the vertical axis, an artifact due to the scan direction. This noise was removed to better resolve the peaks near the origin. The square Te net gives rise to four distinct peaks (L), with peaks related to the CDW oriented at  $45^\circ$ , as indicated by the arrow. The fundamental CDW peak (corresponding to a wavelength of  $\approx 15 \text{ \AA}$ ) and the  $\lambda/2$  harmonic are labeled 1 and 3, respectively. Peaks 2 and 4 are in close proximity to 3, implying a characteristic discommensuration length of  $38 \text{ \AA}$ , as described in the text. Peak 5 corresponds to the diagonal of the Te net. This component may be enhanced due to the underlying crystal structure; the CDW-lattice interaction may also enhance this peak. This figure is in color.

average behavior for a refinement range of around 27 Å (Figure 3.5), which would be expected to occur at around, or a little above, the *radius* of the local domains.

As well as the bond-length distributions, the local and average structure refinements allow us to study the patterns of atomic displacements due to the IC-CDW. The average structure refinement [79] results in an almost perfectly sinusoidal pattern of bond-lengths, with the wavelength of the CDW (Figure 3.8 (a)), clearly identifying these as Peierls distortions. The local structural model was refined in the same unit cell and space-group, but results in a much more square-wave like distribution, consistent with the distinct short and long Te-Te distances described above (Figure 3.8 (b)). Figure 3.8 (c) shows the pattern of Te-Te short-bonds, as defined in the Figure caption, that results when the short distances determined from the PDF data are plotted in the unit cell. In this way, the Peierls distortions are seen to result in oligomers, or short segments of bonded Te atoms, in the Te net. In this picture, the discommensurations occur when the pattern of oligomers has defects. This is a common picture in the chemistry literature [86, 79], though we note that this picture is not supported by the crystallographic results shown in (Figure 3.8 (a)) and needed the application of a local structural method to show that it has a physical reality beyond its heuristic value.

## 3.5 Summary

The refined parameters of the low- $r_{max}$  PDF refinements yield quantitatively the atomic displacements within the commensurate domains. This is the first demonstration of the use of the PDF to obtain quantitatively the atomic displacements (Peierls distortion) within the commensurate domains of a discommensurated IC-CDW. This opens the way to a quantitative first principles calculations and a better microscopic understanding of the IC-CDW state.



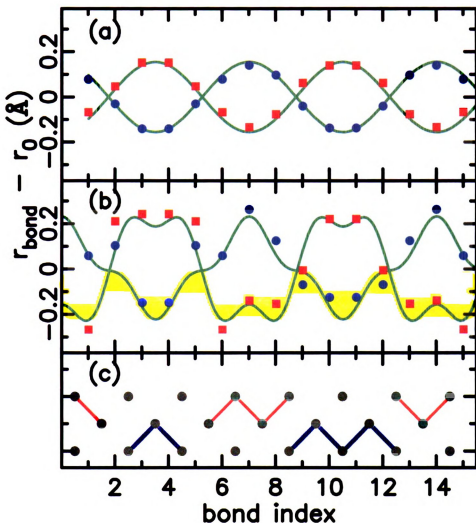


Figure 3.8: Te-Te bond length deviation from the average value as refined crystallographically (a) and from the PDF (b). The deviation  $r_{bond} - r_0$  is defined such that  $r_i$  is the Te-Te bond length of the  $i^{th}$  bond (bond-index  $i$ ) in the unit cell and  $r_0 = 3.1$  Å. (c) Schematic of the arrangements of “short” Te-Te bonds within the unit-cell coming from the PDF refinements and highlighting the formation of oligomers. Red (blue) lines and markers are “short-bonds” lying in the top (bottom) row of the unit cell. Short bonds are defined as those whose length lies within the yellow band in (b). This yellow band is centered at the position of the *first* Gaussian of the bimodal distribution in Figure 3.5 (b) and has a width of one standard deviation of that Gaussian. This figure is in color.

# Chapter 4

## Local Structure of $\text{Zn}_4\text{Sb}_3$ in the $\beta$ phase

H. J. Kim, E. S. Božin, S. M. Haile, G. J. Snyder, and S. J. L. Billinge, **Nano-scale  $\alpha$ -structural domains in the phonon-glass thermoelectric material  $\beta\text{-Zn}_4\text{Sb}_3$** , Phys. Rev. B **75**, 134103 (2007).

### 4.1 Introduction

Only a few materials exhibit the thermoelectric figure of merit  $ZT$  larger than unity and one of those is the  $\beta$  phase of  $p$ -type semiconductor  $\text{Zn}_4\text{Sb}_3$ . This narrow gap semiconductor was discovered in the 1960s [87] and later identified as a thermoelectric material [88]. Ever since then, it has been considered as a state-of-the-art thermoelectric material [87].

#### 4.1.1 Origin of high $ZT$ and phase transitions in $\text{Zn}_4\text{Sb}_3$

$\text{Zn}_4\text{Sb}_3$  exhibits a high thermoelectric performance between 450 K and 670 K (Figure 4.1) and its  $ZT$  value exceeds unity above 540 K [89]. Even though the thermoelectric power factor  $S^2\sigma$  in this temperature range is not so significant compared to

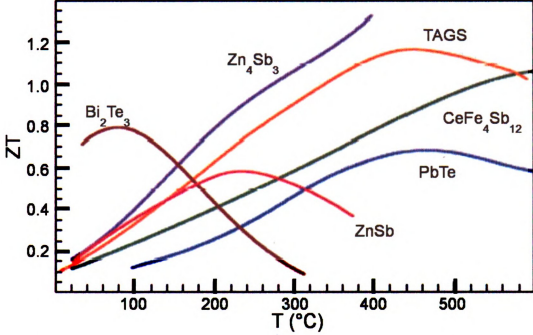


Figure 4.1: Temperature dependence of  $ZT$  value of various thermoelectric materials. Adapted from [89].

that of other thermoelectric materials [90], its very low thermal conductivity, which is comparable to that of glass (Figure 4.2), makes it an excellent thermoelectric material. The typical thermal conductivity value of glass is  $\lesssim 1 \text{ Wm}^{-1}\text{K}^{-1}$  [91]. Since it exhibits good electron conductivity and very low thermal conductivity simultaneously,  $\text{Zn}_4\text{Sb}_3$  is considered as a electron crystal-phonon glass thermoelectric system.

Three modifications of  $\text{Zn}_4\text{Sb}_3$  are known:  $\alpha$ ,  $\beta$ , and  $\gamma$ - $\text{Zn}_4\text{Sb}_3$ . Below  $\sim 260 \text{ K}$  it is in the  $\alpha$  phase (Figure 4.3) and the  $\beta$  phase appears between  $260 \text{ K}$  and  $765 \text{ K}$  [88]. The  $\gamma$  phase is stable in  $765 \text{ K} < T < 857 \text{ K}$  [92]. The high  $ZT$  values are only found in the  $\beta$ -phase. Both phase transitions ( $\alpha \rightarrow \beta$  and  $\beta \rightarrow \gamma$ ) accompany structural changes. The average structure of  $\alpha$ - and  $\beta$ - $\text{Zn}_4\text{Sb}_3$  is low symmetric triclinic ( $C\bar{1}$  space group in monoclinic cell) [87] and high symmetric rhombohedral ( $R\bar{3}c$  space group) structure [93, 92, 89], respectively. These structures will be explored in detail in the next section.

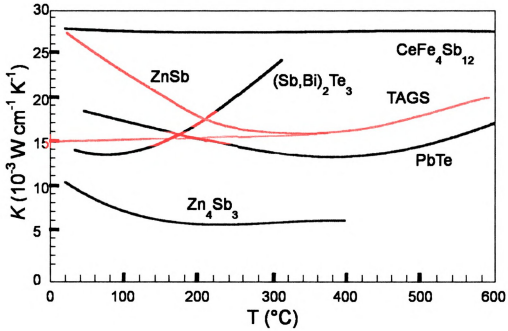


Figure 4.2: Temperature dependence of thermal conductivity of various thermoelectric materials. Adapted from [89].

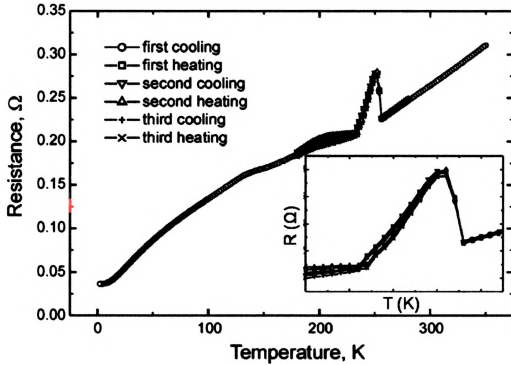


Figure 4.3: Resistance of  $\text{Zn}_4\text{Sb}_3$  as a function of temperature. The inset is a zoom in the  $\alpha \rightarrow \beta$  phase transition region  $\sim 260$  K. Adapted from [92].

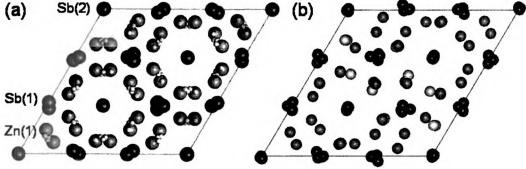


Figure 4.4: The crystal structure of  $\text{Zn}_4\text{Sb}_3$ . (a) Project down the  $c$  axis of the crystal structure of  $\beta\text{-Zn}_4\text{Sb}_3$  in space group  $R\bar{3}c$ . There are three distinct atomic positions, 36Zn(1)b, 18Sb(1), and 12Sb(2). Ionic state for each site is  $\text{Zn}^{2+}$ ,  $\text{Sb}^{3-}$ , and  $\text{Sb}_2^{4-}$  in dimers for 36Zn(1)b, 18Sb(1), and 12Sb(2), respectively. Possible Zn interstitial sites in the interstitial model are indicated with yellow small circles. (b) The interstitial atoms have full occupancy and become ordered in the  $\alpha$ -phase (yellow circles). To help with comparison, only a part of a triclinic supercell is shown. This figure is in color.

#### 4.1.2 Proposed structural models for $\beta\text{-Zn}_4\text{Sb}_3$

The lack of long range order in glass or amorphous structures significantly reduces mean-free paths of phonons by producing strong phonon scattering and consequently very low thermal conductivity is obtained. Electrons are also scattered strongly by the disordered structure resulting in very low electrical conductivity. Therefore, glass is not a good candidate for thermoelectric materials. It is quite amazing that such a low thermal conductivity can be obtained in a crystalline material which still retains good electrical conductivity. Many efforts have been made to search for the structural origin of the exceptionally low thermal conductivity of  $\beta\text{-Zn}_4\text{Sb}_3$ . Several structural defects have been proposed to exist in the rhombohedral  $R\bar{3}c$  structural framework (Figure 4.4 (a)) such as Zn and Sb mixed sites [93] and an occupational deficiency on Zn sites [92]. More recently, interstitial Zn atom defects are reported [89, 94]. Interstitial Zn atoms are randomly distributed over multiple crystallographic sites in the crystal structure of  $\beta\text{-Zn}_4\text{Sb}_3$  (small yellow circles in Figure 4.4 (a)). Three  $\beta$ -phase structural models are summarized in Table 4.1. Soon after the discovery of intersti-

Table 4.1: Site occupancies (fraction) for various  $\beta$ - $\text{Zn}_4\text{Sb}_3$  structural models based on the  $R\bar{3}c$  structural framework.

model	Zn(1) (36f)	Sb(1) (18e)	Sb(2) (12c)	Zn-interstitial (36f)
Mixed occupancy	1	0.89Sb 0.11Zn	1	0
Vacancy	0.90	1	1	0
Interstitial	0.90	1	1	0.17 0.046Zn(2) 0.056Zn(3) 0.063Zn(4)

tial defects in the  $\beta$  phase, superlattice peaks due to the ordering of Zn interstitial defects were observed in the  $\alpha$  phase [87, 95]. Ordered interstitials quadruple the cell along the [011] direction of the rhombohedral cell. A part of the supercell is shown in Figure 4.4 (b). In this structure, all the sites are fully occupied including interstitial sites (yellow circles). The Zn substructure of the  $\alpha$  phase is strongly locally deviated from that of the  $\beta$  phase whereas the Sb substructures differ only fractionally [87]. The mechanism and true nature of this order-disorder ( $\alpha \rightarrow \beta$ ) transition, which takes place at rather low temperatures and turns out to be reversible, is still not fully understood [87].

## 4.2 Experimental details

### 4.2.1 Experiment and data process

Two  $\text{Zn}_4\text{Sb}_3$  samples (I and II) were prepared at different times by direct reaction of the elements. The phase purity of each sample was checked by powder x-ray diffraction and scanning electron microscopy with energy dispersive spectroscopy. No traces of  $\text{ZnSb}$  or  $\text{Zn}$  were found by either method.

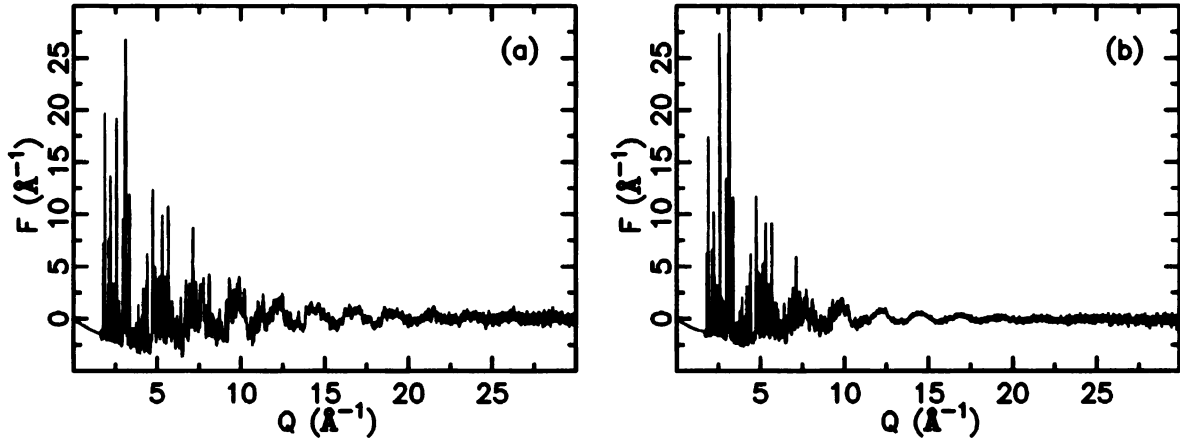


Figure 4.5: The reduced total scattering structure function,  $F(Q)$  of  $\text{Zn}_4\text{Sb}_3$  obtained from neutron data at (a) 15 K ( $\alpha$  phase) and (b) 300 K ( $\beta$  phase).

Neutron powder diffraction measurements were carried out on the NPDF (Neutron Powder Diffractometer) at the Lujan Center at Los Alamos National Laboratory. About 8.0 g of powder sample I was sealed in a cylindrical vanadium can under helium exchange gas. Data were collected using a displac closed cycle refrigerator at 15 K and 300 K. Using the program PDFgetN [58] various corrections [49] including background subtraction (empty vanadium can) were made and the neutron PDFs were obtained by Fourier transform of the reduced total scattering structure function,  $F(Q)$  (Figure 4.5) up to  $Q_{max}$  of  $30 \text{ \AA}^{-1}$ .

X-ray powder diffraction data for sample II were collected at room temperature and over a range of temperatures to 150 K at the 6-IDD station of MUCAT beamline at the Advanced Photon Source at Argonne National Laboratory. The sample was ground using a mortar and pestle, sieved through a 400-mesh sieve, and then loaded in a flat-plate aluminium sample holder with thickness of 1.0 mm sealed with kapton tape. The x-ray energies were 87.005 keV ( $\lambda = 0.14248 \text{ \AA}$ ) for the 300 K data and 129.77 keV ( $\lambda = 0.095541 \text{ \AA}$ ) for the low temperature measurements. Data were collected using the rapid acquisition pair distribution function (RAPDF) technique, which utilizes a two-dimensional image plate detector (Mar345) 345 mm in diameter [54]. The camera was mounted orthogonally to the beam path. The sample-to-

detector distance for each experiment was determined by calibrating with a silicon standard sample: 210.00 mm and 218.87 mm for 87.005 keV and 129.77 keV, respectively. Low temperature measurements were carried out by using low temperature displax with a mylar heat-shield and kapton windows. An empty sample holder under the 300 K and low temperature setup was measured for background. Upon reaching the target temperature, the system was allowed to equilibrate for 10 minutes prior to data collection. In order to avoid saturation of the detector, sample was exposed to x-ray beam for 10 seconds (120 seconds) and it was repeated eight times (seven times) to improve the counting statistics for 300 K (low temperature) measurements. One of raw image data sets obtained at 300 K is shown in Figure 4.6 (a).

Two-dimensional data sets corresponding to each temperature were further combined and integrated using the program FIT2D [56] to obtain intensity versus  $2\theta$  format. Background subtraction and standard corrections [54, 49] were made using the program PDFgetX2 [57] to obtain  $F(Q)$  which was truncated at  $Q_{max}$  of  $28 \text{ \AA}^{-1}$  before performing Fourier transformation to obtain the x-ray PDF. Beyond that value of  $Q$  the signal-to-noise ratio was unfavorable.  $F(Q)$  at 300 K is shown in Figure 4.6 (b).

## 4.2.2 Structural Modeling

Three structural models based on the  $R\bar{3}c$  framework (mixed occupancy, [93] vacancy, [92] and interstitial [89] models) and the  $\alpha$ -phase superstructure were used for this study (Table 4.1). The  $\alpha$ -phase superstructure, here named the  $\alpha$ -structural model, accounts for superlattice peaks arising from ordered Zn interstitial defects below  $T \approx 260 \text{ K}$  [87, 95].

The structural modeling was carried out using the program PDFFIT2 [60]. Each model was taken as an initial structure then lattice parameters, atomic coordinates and isotropic displacement parameters ( $U_{iso}$ ) were refined using a least squares ap-



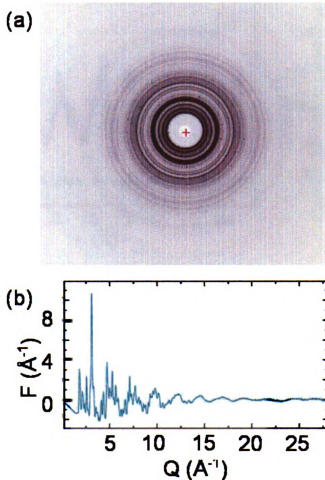


Figure 4.6: (a) An example of a raw image data set of  $\text{Zn}_4\text{Sb}_3$  obtained at 300 K and (b)  $F(Q)$  for 300 K x-ray data.

proach until the difference between the experimental and calculated PDFs was minimized. The atomic coordinates were constrained to retain the symmetry of the  $R\bar{3}c$  space group for the mixed occupancy, vacancy, and interstitial models. For the  $\alpha$ -structural model, the space group  $C\bar{1}$  was used and the atomic coordinates were fixed to the values from the literature [87]. For all the models only two parameters were assigned for  $U_{iso}$ ; one for Zn atoms and the other for Sb atoms regardless of different crystallographic sites. The refinement range was  $1.5 < r < 20.0 \text{ \AA}$ .

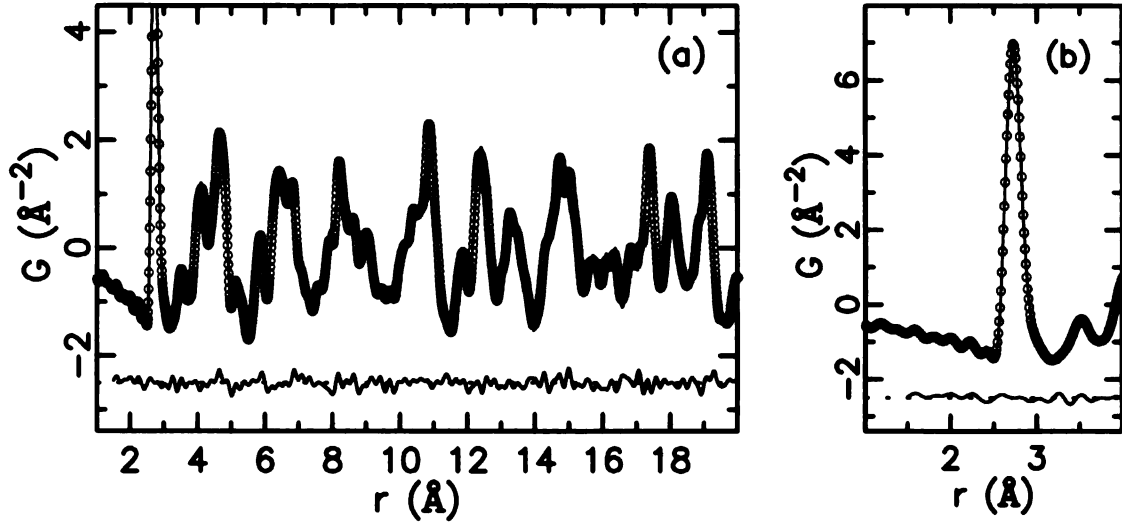


Figure 4.7: 15 K neutron PDF refinement result. (a) The experimental PDF obtained at 15 K (blue circles) together with the calculated PDF from the refined  $\alpha$ -model (red line). The difference between the calculated and measured PDFs (green line) is plotted below the data. (b) Zoom in to the first PDF peak. This figure is in color.

## 4.3 Results

### 4.3.1 Local structure of $\text{Zn}_4\text{Sb}_3$ in $\alpha$ -phase

The PDF obtained from 15 K neutron data is shown with blue circles in Fig. 4.7. The excellent signal to noise ratio of the data is evident from the negligibly small ripples on the base line of the PDF below 2  $\text{\AA}$ , compared to the PDF peaks. The first sharp peak at 2.7  $\text{\AA}$  derives from the nearest-neighbor pairs of Zn-Zn, Zn-Sb, and Sb-Sb in the rhombohedral unit cell (Fig. 4.4 (a)). The calculated PDF from the refined  $\alpha$ -structural model (red line) is plotted over the data with the difference (green line) shown in the curve below it. The refined values of the structural parameters are summarized in Table 4.2. The model is in excellent agreement with the data without refinement of atomic coordinates, directly indicating that the local structure agrees well with the average structure in the  $\alpha$ -phase.

Table 4.2: Refined structural parameters from various models. Lattice parameters and isotropic displacement parameters ( $U_{iso}$ ) were refined for all models. The atomic coordinates (not reported here) were refined only for mixed occupancy, vacancy and interstitial models being constrained to keep the  $R\bar{3}c$  symmetry. The refinement range was  $1.5 < r < 20.0 \text{ \AA}$ .

	Mixed Occupancy			Vacancy			Interstitial			$\alpha$ -structural		
	neutron 300 K	x-ray 300 K	neutron 300 K	neutron 300 K	x-ray 300 K	neutron 300 K	neutron 300 K	x-ray 300 K	neutron 300 K	x-ray 300 K	neutron 300 K	neutron 15 K
$a$ (Å)	12.2508(5)	12.231(2)	12.2444(5)	12.244(1)	12.244(1)	12.2433(5)	12.234(2)	32.730(7)	32.576(3)	32.553(5)		
$b$ (Å)								12.249(3)	12.220(6)	12.236(2)		
$c$ (Å)	12.432(1)	12.468(3)	12.430(1)	12.472(1)	12.464(1)	10.896(3)	98.97(1)	99.25(1)	10.945(1)	10.872(2)		
$\beta$											98.99(1)	
Zn $U_{iso}$ (Å <sup>2</sup> )	0.0333(2)	0.0459(1)	0.0315(2)	0.0731(3)	0.0269(2)	0.0292(3)	0.0176(1)	0.0285(2)	0.0052(1)			
Sb $U_{iso}$ (Å <sup>2</sup> )	0.01191(9)	0.0151(1)	0.0147(1)	0.0110(3)	0.0140(1)	0.0166(1)	0.0098(1)	0.0126(1)	0.00281(7)			
$n^a$	9	9	9	9	18	18	6	6	6	6		
$R_w$	0.153501	0.14236	0.150178	0.162943	0.123122	0.116389	0.138129	0.0835491				
$R_w^b$	0.268002	0.242116	0.258401	0.291704	0.227926	0.133564	0.159292					

<sup>a</sup>Number of parameters used.

<sup>b</sup>Results with  $U_{iso}$  for both Zn and Sb atoms fixed to  $0.01 \text{ \AA}^2$ .

### 4.3.2 Local structure of $\text{Zn}_4\text{Sb}_3$ in $\beta$ -phase

Now we focus on the PDF of  $\beta\text{-Zn}_4\text{Sb}_3$ . The results of structural modeling on the neutron PDF at 300 K using the mixed occupancy, vacancy, and interstitial models are summarized in Table 4.2. Reasonably good fits are obtained from each of the models (Figure 4.8 (a)~(c)) with agreement factor,  $R_w$ , [60] of around 0.15 for mixed occupancy and vacancy models and lower for the interstitial model which has 2 ~ 3 times more refinable parameters. These good fits are obtained at the expense of enlarged atomic displacement factors on the Zn sites, though the interstitial model does better in this regard. Enlarged atomic displacement factors may signify the presence of loosely coordinated “rattler ions”, [96] or alternatively non-thermal disorder that is not incorporated explicitly in the models.

The  $R_w^b$  values in Table 4.2 show how the results changed when  $U_{iso}$  was fixed to a smaller value of  $0.01 \text{ \AA}^2$ , a value between the refined 15 K and 300 K values and appropriate for a temperature in the vicinity of the structural phase transition, for both Zn and Sb atoms. Now the insufficiency of each model emerges due to the sharpening of PDF peaks by the small  $U_{iso}$  value (Figure 4.9 (a)~(c)). The results imply that the local structure of  $\beta\text{-Zn}_4\text{Sb}_3$  is somehow more distorted than the three models suggest.

We also tried the  $\alpha$ -structural model for the *local* structure of the 300 K data. It provides as good a fit as the other models did with just  $U_{iso}$  being refined (Figure 4.8 (d)). With fewer parameters the resultant  $R_w$  value is comparable to the other models (Table 4.2). The most interesting result was obtained when  $U_{iso}$  was fixed to  $0.01 \text{ \AA}^2$  during the refinement (Figure 4.9 (d)). Even though  $U_{iso}$  was fixed, a good fit was still obtained; the fluctuation in the difference curve is not significant and most of all, the  $R_w$  value does not change much (Table 4.2) implying that in the  $\beta$ -phase the  $\alpha$ -like structure is preserved locally. This result suggests that the enlarged  $U_{iso}$  on Zn sites in the  $\beta$ -model is due to averaging of different local environments in the

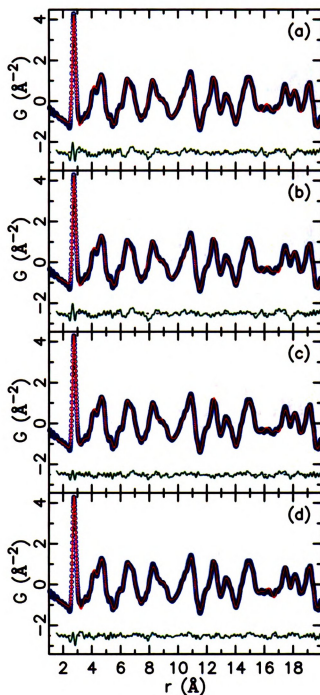


Figure 4.8: 300 K neutron PDF refinement results. The experimental PDF obtained at 300 K (blue circles) are plotted with the calculated PDF (red line) from various refined structural models; (a) mixed occupancy model, (b) vacancy model, (c) interstitial model, and (d)  $\alpha$ -structural model. The difference (green line) is plotted below the data. This figure is in color.

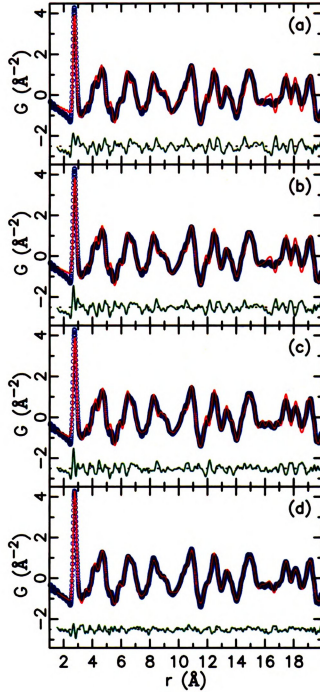


Figure 4.9: 300 K neutron PDF refinement results with fixed  $U_{iso}$  value of  $0.01 \text{ \AA}^2$ . The experimental PDF (blue circles) are plotted with the calculated PDF (red line) from refined (a) mixed occupancy model, (b) vacancy model, (c) interstitial model, and (d)  $\alpha$ -structural model. The difference (green line) is plotted below the data. The good agreement in (d) indicates that the  $\alpha$ -structural model explains the *local* structure of  $\beta\text{-Zn}_4\text{Sb}_3$  with a smaller value of  $U_{iso}$  whereas other models do not (a)-(c). This figure is in color.

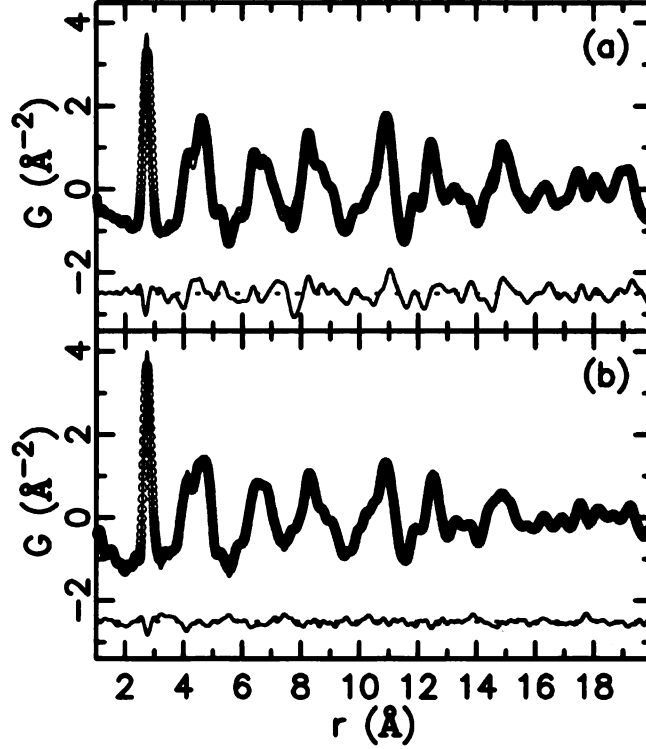


Figure 4.10: Comparison of the change in PDF expected as the sample goes from the  $\alpha$  to  $\beta$  phase. The PDF in the  $\alpha$  phase is shown in red line and the  $\beta$ -phase in blue circles. The difference is plotted below in green line. (a) The *calculated* PDFs based on the average structures.  $U_{iso}$  used for the calculation is  $0.01 \text{ \AA}^2$  for both interstitial and  $\alpha$ -structural models. (b) *Experimental* x-ray PDFs in  $\beta$  (270 K, blue circles) and  $\alpha$  (220 K, red line) phases. The observed changes in the local structure are much smaller than expected from the crystal structure models. This figure is in color.

cubic model and interstitials are not rattler ions.

As a further check of this hypothesis we measured the temperature dependence of the local structure through the  $\alpha$ - $\beta$  phase transition at 260 K. Indeed, there is no significant change in the x-ray PDF on crossing the transition (Figure 4.10 (b)), compared to the expected change based on the  $\alpha$  and  $\beta$  models (Figure 4.10 (a)), indicating that locally the structure is not changing even though there is a change in the average symmetry at this transition. For the calculation the  $\alpha$ -structural and interstitial models were adopted representing the  $\alpha$  and  $\beta$  phase, respectively.  $U_{iso}$  of  $0.01 \text{ \AA}^2$  was used for both models assuming that the thermal effect is relatively small compared to the structural change in this temperature range.

## 4.4 Discussion

### 4.4.1 What is in the $\alpha$ -structural model?

It is interesting to investigate what aspect of the  $\alpha$ -model makes it better for the low- $r$  region of the PDF of  $\beta$ - $\text{Zn}_4\text{Sb}_3$  than the interstitial model even though they have similar numbers of Zn interstitial atoms. The improvement in fit is unlikely to be explained by the ordering arrangement of interstitial atoms in the  $\alpha$ -model since the defects themselves are only 10 % in the fully occupied  $R\bar{3}c$  framework [89, 87] and the consequent effect is small in the PDF. The reason seems to lie in the local coordination of the interstitial atoms in the respective models. The interstitial model provides possible Zn interstitial sites in a highly symmetric  $R\bar{3}c$  structural frame (Figure 4.4 (a)) but not their influence of relaxing the positions of neighboring atoms. Accordingly, large  $U_{iso}$  values are necessary for the interstitial model to get sufficiently broad PDF peaks. However, the lower symmetry atomic arrangement in the  $\alpha$ -model (Figure 4.4 (b)) correctly captures the perturbed environment of the interstitial atoms. Since the local structure does not change at the  $\alpha$ - $\beta$  phase transition the Zn interstitial defects persist but lose their long-range order forming the  $\alpha$ -like domains in the  $\beta$ -phase.

When point defects are discovered in a material, particularly charged point defects that require other charge balancing defects, one should expect local structural distortions or rearrangements that will lead, either to long range order and a superstructure, or to short-range ordered nanometer size domains that are not detected with traditional diffraction techniques. In the  $\text{Zn}_4\text{Sb}_3$  case, the Zn interstitials order at low temperature resulting in a new crystallographic phase and a superstructure in the diffraction pattern [87, 95]. This tendency to order locally will reduce coulombic and elastic strain energies. At high temperature the defects prefer to disorder to increase the entropy, but the strong tendency towards local ordering persists resulting



in nanoscale domains, or short-range order with a finite coherence length, such as was found here.

#### 4.4.2 Domain size estimation

In the  $\beta$ -phase the local  $\alpha$ -like domains must be oriented in such a way that crystallographically the interstitial atoms appear in a randomly distributed way over three possible interstitial sites in the average  $R\bar{3}c$  structure. However, the similarity of the local structure suggests that locally the interstitial atoms avoid each other in the  $\beta$ -phase resulting in short-range defect ordering that resembles the  $\alpha$  phase. A possible picture of  $\beta$ - $\text{Zn}_4\text{Sb}_3$  structure is depicted in the upper part of Figure 4.11: the structure consists of many  $\alpha$ -structural like domains and the direction of ordering of Zn interstitial defects in each domain is indicated by the orientation of yellow lines. The rhombohedral  $\beta$ -structure is incomplete as a local structure as it has atomic distances that are unphysically short. This work confirms that the actual local structure contains reasonable atomic distances (such as those in the  $\alpha$ -phase with no indication of a Zn-Zn bond [94]) and that nano-scale domains must exist. We would like to estimate the domain size, or coherence length, of this local order. At low- $r$  the PDF is probing below this domain length scale and finds an  $\alpha$ -like local structure (Figure 4.11 (a)); however, the PDF at high- $r$  (consistent with the average x-ray diffraction measurements [89]) averages over a longer length scale and results in the different average structure of  $\beta$ - $\text{Zn}_4\text{Sb}_3$  (Figure 4.11 (b)). A striking feature found in a comparison of the 300 K and 15 K neutron PDFs is an inversion of the relative PDF peak heights in the region between 60-120 Å (Figure 4.12). Below 60 Å the PDF peaks in the 15 K data are taller than those in the 300 K data (Figure 4.12 (b)), as expected due to the reduced thermal motion. However, above 120 Å the opposite is observed (Figure 4.12 (d)). If there is no phase change the PDF peaks will broaden with increasing temperature at all distances- $r$ , but this is not observed. The

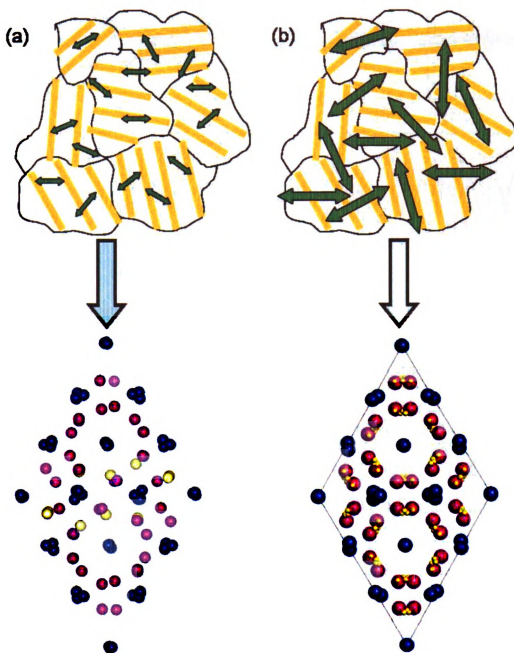


Figure 4.11: A possible picture of  $\beta\text{-Zn}_4\text{Sb}_3$  structure. The structure is composed of many  $\alpha$ -like domains with Zn interstitial atoms ordered along the yellow lines. (a) Local structural probes such as PDF provides  $\alpha$ -like structure whereas (b) crystallography averages over domains providing three possible Zn interstitial sites with partial occupancies. This figure is in color.

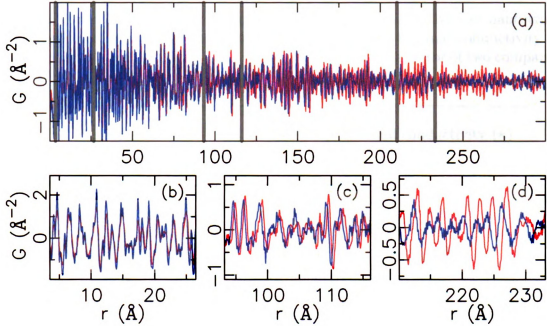


Figure 4.12: Comparison of 15 K and 300 K PDFs in different  $r$ -regions. (a) Comparison of low- (15 K, blue line) and high-temperature (300 K, red line) neutron PDFs of  $\text{Zn}_4\text{Sb}_3$  plotted over a wide range of  $r$  to 300  $\text{\AA}$ . (b)-(d) are the same data but plotted on expanded  $r$ -scales. Note that at low- $r$  the 300 K PDF has broader and lower peaks, but at high- $r$  the situation is reversed. PDF peaks broaden with temperature due to increased thermal motion as evident at low- $r$  (b). The PDF peaks are sharper and higher at room temperature in the high- $r$  region (d) because the 300 K data are from the high-symmetry  $\beta$ -phase. A rough estimate of the size of the local  $\alpha$  domains can be obtained from the where the behavior switches over (c). This figure is in color.

anomalous T-dependence is explained due to the fact that at higher- $r$  the PDF reflects the higher symmetry of the  $\beta$ -structure and higher symmetry results in sharper PDF peaks. The fact that the low- $r$  peaks broaden with increasing temperature and do not sharpen at the phase transition is strong evidence that the local symmetry is lower than the average symmetry. We can roughly estimate the diameter of the lower symmetry domains from the crossover in peak-broadening behavior. The crossover happens in the region 60-120  $\text{\AA}$  (Figure 4.12 (c)). We therefore estimate the  $\alpha$ -domain size to be of the order, but probably somewhat less than, 10 nm, where the effects on the PDF of the higher average symmetry start to dominate. A more thorough study is necessary to estimate the exact domain size.

Table 4.3: Comparison of the size of defects and thermal conductivity of nanostructured thermoelectric systems and  $\beta$ -Zn<sub>4</sub>Sb<sub>3</sub> at 300 K. The thermal conductivity of ErAs nanoparticles embeded In<sub>0.53</sub>Ga<sub>0.47</sub>As was reduced by a factor of two compared to that of In<sub>0.53</sub>Ga<sub>0.47</sub>As.

system	defects size (nm)	thermal conductivity ( $\kappa$ ) (Wm <sup>-1</sup> K <sup>-1</sup> )
Bi <sub>2</sub> Te <sub>3</sub> /Sb <sub>2</sub> Te <sub>3</sub> [42]	1 nm/5 nm	$\sim 0.25$
Ag(Pb <sub>1-y</sub> Sn <sub>y</sub> ) <sub>m</sub> SbTe <sub>2+m</sub> [48]	$\sim 3$ nm	$\sim 0.7$
ErAs/In <sub>0.53</sub> Ga <sub>0.47</sub> As [41]	$1 \sim 4$ nm	$\sim 3 (\times 0.5)$
$\beta$ -Zn <sub>4</sub> Sb <sub>3</sub>	$6 \sim 12$ nm	$\sim 1$

#### 4.4.3 Possible role of $\alpha$ -structural like nanodomains in thermal conductivity of $\beta$ -Zn<sub>4</sub>Sb<sub>3</sub>

The PDF study has suggested that the structure of high  $ZT$   $\beta$  form of Zn<sub>4</sub>Sb<sub>3</sub> is composed of nanoscaled  $\alpha$ -like domains. Do these nano-domains play an important role in the low thermal conductivity of  $\beta$ -Zn<sub>4</sub>Sb<sub>3</sub>?

Several recently developed nanostructured thermoelectric systems were introduced in the section 1.3.3. In all these systems nanoscale structural [42, 41] or compositional modulations [48] of  $1 \sim 6$  nm appear to play an important role in huge reduction of thermal conductivity. Table 4.3 summarizes the size of nanoscale defects and thermal conductivity found in each system together with  $\beta$ -Zn<sub>4</sub>Sb<sub>3</sub>. Our PDF analysis shows that the structure of high  $ZT$   $\beta$ -Zn<sub>4</sub>Sb<sub>3</sub> consists of  $\alpha$ -structure like domains with  $6 \sim 12$  nm size. The compelling similarity in the order of domain size to nanoscale structural modulations in other high  $ZT$  materials (Table 4.3) strongly suggests their important role in very low thermal conductivity of  $\beta$ -Zn<sub>4</sub>Sb<sub>3</sub>. One different thing between  $\beta$ -Zn<sub>4</sub>Sb<sub>3</sub> and other systems here is that  $\beta$ -Zn<sub>4</sub>Sb<sub>3</sub> is chemically a homogeneous material whereas the other nanostructured systems are two-phase systems.

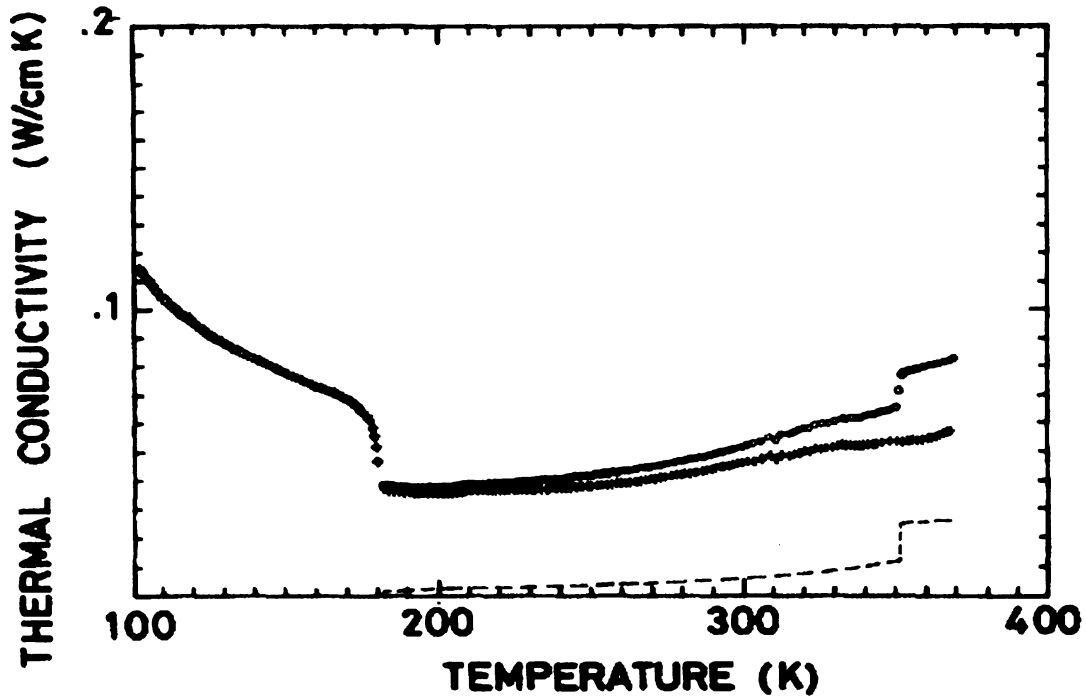


Figure 4.13: The basal thermal conductivity of  $1T$ -TaS<sub>2</sub> as a function of temperature. Open circles represent experimental results and dashed line is electronic contribution from Wiedeman-Franz law. Estimated lattice contribution is plotted in crosses. Adapted from [97]

Therefore, phonons are scattered at heterogeneous interfaces in these nanostructured materials but at domain boundaries in  $\beta$ -Zn<sub>4</sub>Sb<sub>3</sub>. One thing we need to check is how effectively domain boundaries can reduce thermal conductivity of materials. One good example to examine this matter is a charge density wave (CDW) system which has nearly commensurate to commensurate CDW transition. Figure 4.13 shows the basal thermal conductivity of  $1T$ -TaS<sub>2</sub> measured during cooling [97]. Nearly commensurate to commensurate CDW transition occurs at 180 K. Commensurate CDW domains with  $\sim 6$  nm in size are separated by domain walls called discommensurations in the nearly commensurate CDW state,  $180 \text{ K} < T < 350 \text{ K}$ . Notice how rapidly the thermal conductivity of  $1T$ -TaS<sub>2</sub> changes at this transition; it is increased by nearly a factor of two in the commensurate CDW state,  $T < 180 \text{ K}$ . Núñez-Regueiro *et al.* suggested that the disappearance of defects (discommensurations) in the commensurate CDW state as one possible explanation for this huge change in thermal

conductivity of  $1T$ -TaS<sub>2</sub> across the transition.

## 4.5 Summary

We have investigated the local structure of Zn<sub>4</sub>Sb<sub>3</sub> using the PDF technique. The result shows that the structure of  $\beta$ -Zn<sub>4</sub>Sb<sub>3</sub> at 300 K is composed of nanoscaled  $\alpha$ -like domains. Like other recently developed high  $ZT$  thermoelectric materials, the exceptionally low thermal conductivity of  $\beta$ -Zn<sub>4</sub>Sb<sub>3</sub> may be attributed to these nanoscale structural domains.

# Chapter 5

## Concluding Remarks

### 5.1 Summary

#### 5.1.1 $\text{CeTe}_3$

Incommensurate charge density waves (IC-CDW) are a fundamental property of low-dimensional metals. Knowing the nature of local atomic displacements (Peierls distortions) in the IC-CDWs is crucial to understand novel properties of many materials, but this information is difficult to obtain quantitatively. We have applied a local structural method, the atomic pair distribution function (PDF) technique, to determine the local atomic displacements in the system  $\text{CeTe}_3$ . IC-CDWs, and the underlying atomic displacements, can be uniform incommensurate modulations or locally commensurate waves separated by narrow domain walls, known as discommensurations, where the phase of the wave changes rapidly. The IC-CDWs lie in the nominally square Te layers in  $\text{CeTe}_3$ . The PDF analysis on 300 K data showed that the Te-Te bonds found in the square Te layers split into short bonded or long non-bonded parts. Since this is the characteristic feature of commensurate CDW, the IC-CDW in  $\text{CeTe}_3$  at 300 K is discommensurated. This is the first time the quantitative local atomic displacements have been obtained within the commensurate domains of a

discommensurated IC-CDW.

### 5.1.2 $\beta$ -Zn<sub>4</sub>Sb<sub>3</sub>

$\beta$ -Zn<sub>4</sub>Sb<sub>3</sub> is an excellent example of a “phonon-glass” thermoelectric material but the mechanism for its low thermal conductivity is not fully established. We used the atomic pair distribution function (PDF) analysis of x-ray and neutron scattering data to study the local structure of  $\beta$ -Zn<sub>4</sub>Sb<sub>3</sub>. We showed that interstitial Zn atoms not only provide point defects but also force a local structural rearrangement on the nanometer scale in  $\beta$ -Zn<sub>4</sub>Sb<sub>3</sub>. Locally, the material retains its low-symmetry low-temperature form and the higher symmetry average structure of  $\beta$ -Zn<sub>4</sub>Sb<sub>3</sub> is due to averaging of these nanometer scale local domains. Temperature-dependent measurements through the  $\alpha$ - $\beta$  transition support this picture. We have estimated the domain size at less than 10 nm from a comparison of low- and high-temperature PDFs determined over a wide range of  $r$ . These intrinsically self-organized nano-domains should effectively scatter the mid- to long-wavelength phonons that are important for heat transport. Interestingly, the observation of nano-domains in the high  $ZT$   $\beta$ -form of the material is consistent with the emerging theme of producing materials with nanoscale superstructures or defects to efficiently scatter mid- to long-wavelength phonons to achieve high  $ZT$  value.

## 5.2 Importance of local structures for understanding material properties

The local atomic arrangements of CeTe<sub>3</sub> and Zn<sub>4</sub>Sb<sub>3</sub> determined from the PDF analysis are different from ones that conventional crystallography provides. The local orderings extend over nanometer-length scales in both materials forming nano-domains and crystallography averages out these domains yielding somehow different structures.



This is not rare [3], but is often found in various materials such as manganites [98, 99], ferroelectrics [100], thermoelectric materials [41, 44, 46], and so on, and is expected to play an important role in material properties. Many further detailed research works using various techniques need to be done on these nano-scaled clusters to understand their exact role.

## 5.3 Future Work

### 5.3.1 Fluctuation effects in $\text{RETe}_3$

Large gaps associated with CDWs are found in  $\text{RETe}_3$  (RE=rare earth). For example the mean field CDW transition temperature of  $\text{SmTe}_3$ , determined by the gap obtained from Angle-resolved photoemission spectroscopy (ARPES) study, is  $\approx 1300$  K, which is larger than its melting temperature, 1096 K [80]. However, in reality the CDW phase transition occurs at 415 K in  $\text{SmTe}_3$  where long range order develops resulting in superlattice peaks. This suggests the importance of fluctuation effects [4] in this system and the possible existence of short range ordered CDW regions above 415 K. By collecting data in a wide temperature range below and above  $T_{CDW}$  and using PDF analysis, a novel local structure probing method, fluctuation effects and the developement of CDWs in  $\text{RETe}_3$  system can be closely investigated.

### 5.3.2 Nano-domains in $\beta\text{-Zn}_4\text{Sb}_3$ in the high T region

It can not be said "the nano-domains found in this study are directly responsible for the very low thermal conductivity of  $\beta\text{-Zn}_4\text{Sb}_3$ " at this moment, but we believe that there must be a close connection between them.  $\beta\text{-Zn}_4\text{Sb}_3$  exhibits high thermoelectric performance (high  $ZT$  values) between 450 K and 670 K. Its  $ZT$  value exceeds unity above 540 K. Therefore, in order to make our argument clear a thorough study on the evolution of the domain size with temperature up to the high  $ZT$  regime (above

540 K) is required. In addition, more precise ways to estimate the domain size are necessary. One possible way is to systematically increase the refinement range (fix  $r_{min}$  and vary  $r_{max}$ ). The domain size can be determined where refined parameters start deviated from the trend. However, this requires high computing power and huge amount of time since refinement should be carried out over a wide  $r$ -range using a large structural model.

# Bibliography

- [1] P. G. Collins and P. Avouris, **Nanotubes for Electronics**, Scientific American , 62 (2000).
- [2] V. K. Pecharsky and P. Y. Zavalij, *Fundamentals of Powder Diffraction and Structural Characterization of Materials*, Springer, New York, USA, 2005.
- [3] S. J. L. Billinge and I. Levin, **The problem with determining atomic structure at the nanoscale**, Science **316**, 561 (2007).
- [4] G. Grüner, *Density Waves in Solids*, Addison-Wesley, New York, 1994.
- [5] R. E. Peierls, *Quantum Theory of Solids*, Clarendon Press, Oxford, England, 1955.
- [6] M. J. Rice and S. Strässler, **Effects of fluctuations and interchain coupling on the Peierls transition**, Solid State Commun. **13**, 1389 (1973).
- [7] W. L. McMillan, **Theory of discommensurations and commensurate-incommensurate charge-density wave-phase transition**, Phys. Rev. B **14**, 1496 (1976).
- [8] W. L. McMillan, **Collective modes of a charge-density wave near lock-in transition**, Phys. Rev. B **16**, 4655 (1977).
- [9] D. E. Moncton, J. D. Axe, and F. J. Disalvo, **Study of superlattice formation in 2H-NbSe<sub>2</sub> and 2H-TaSe<sub>2</sub> by neutron-scattering**, Phys. Rev. Lett. **34**, 734 (1975).
- [10] A. M. Gabovich, A. I. Voitenko, and M. Ausloos, **Charge- and spin-density waves in existing superconductors: competition between Cooper pairing and Peierls or excitonic instabilities**, Phys. Rep. **367**, 583 (2002).
- [11] E. Morosan, H. W. Zandbergen, B. S. Dennis, J. W. G. Bos, Y. Onose, T. Klimczuk, A. P. Ramirez, N. P. Ong, and R. J. Cava, **Superconductivity in Cu<sub>x</sub>TiSe<sub>2</sub>**, Nature Phys. **2**, 544 (2006).
- [12] S. Nagata, T. Aochi, T. Abe, S. Ebisu, T. Hagino, Y. Seki, and K. Tsutsumi, **Superconductivity in the layered compound 2H-TaS<sub>2</sub>**, J. Phys. Chem. Solids **53**, 1259 (1992).
- [13] B. Mihaila et al., **Pinning Frequencies of the Collective Modes in  $\alpha$ -Uranium**, Phys. Rev. Lett. **96**, 076401 (2006).

- [14] D. Jaiswal, A. A. Tulapurkar, S. Ramakrishnan, A. K. Grover, G. J. Nieuwenhuys, and J. A. Mydosh, **Superconducting parameters of a CDW compound  $\text{Lu}_5\text{Ir}_4\text{Si}_{10}$** , *Physica B* **312**, 142 (2002).
- [15] Y. Singh, R. Nirmala, S. Ramakrishnan, and S. K. Malik, **Competition between superconductivity and charge-density-wave ordering in the  $\text{Lu}_5\text{Ir}_4(\text{Si}_{1-x}\text{Ge}_x)_{10}$  alloy system**, *Phys. Rev. B* **72**, 045106 (2005).
- [16] T. Kiss, T. Yokoya, A. Chainani, S. Shin, T. Hanaguri, M. Nohara, and H. Takagi, **Charge-order-maximized momentum-dependent superconductivity**, *Nature Phys.* **3**, 720 (2007).
- [17] J. Zaanen, S. Chakravarty, T. Senthil, P. Anderson, P. Lee, J. Schmalian, M. Imada, D. Pines, M. Randeria, C. Varma, M. Vojta, and M. Rice, **Towards a complete theory of high  $T_c$** , *Nature Phys.* **2**, 138 (2006).
- [18] D. M. Rowe, editor, *CRC Handbook of Thermoelectrics*, Chemical Rubber Press, Boca Raton, FL, 1995.
- [19] M. G. Kanatzidis, S. D. Mahanti, and T. P. Hogan, *Chemistry, Physics, and Materials Science of Thermoelectric Materials: Beyond Bismuth Telluride*, Kluwer Academic/Plenum Publishers, 2002.
- [20] T. M. Tritt and M. A. Subramanian, **Thermoelectric materials, phenomena, and applications: A bird's eye view**, *MRS Bulletin* **31**, 188 (2006).
- [21] G. S. Nolas, J. Sharp, and H. J. Goldsmid, *Thermoelectrics: basic principles and new materials developments*, Springer-Verlag, 2001.
- [22] T. J. Seebeck, **Magnetische Polarisation der Metalle und Erzedurch Temperatur-Differenz.Abhand**, *Deut. Akad. Wiss. Berlin* , 265 (1822).
- [23] H. J. Goldsmid, *Applications of thermoelectricity*, Methuen, London, England, 1960.
- [24] J. M. Ziman, *Principles of the Theory of Solids*, Cambridge University Press, Cambridge, England, 1972.
- [25] N. W. Ashcroft and N. D. Mermin, *Solid State Physics*, Holt, Rinehart and Winston, New York, USA, 1976.
- [26] J. C. Peltier, **Nouvelles experiences sur la caloricete des courans electriques**, *Ann. Chem.* **LVI**, 371 (1834).
- [27] W. Thomson, **On a mechanical theory of thermoelectric currents**, *Proc. Roy. Soc., Edinburgh* , 91 (1851).
- [28] F. J. DiSalvo, **Thermoelectric cooling and power generation**, *Science* **285**, 703 (1999).

- [29] G. A. Slack, **New materials and performance limits for thermoelectric cooling**, in *CRC Handbook of Thermoelectrics*, edited by D. M. Rowe, chapter 34, Chemical Rubber, Boca Raton, FL, 1995.
- [30] G. S. Nolas, J. Poon, and M. Kanatzidis, **Recent Developments in Bulk Thermoelectric Materials**, Mater. Res. Soc. Bull. **31**, 199 (2006).
- [31] B. C. Sales, D. Mandrus, and R. K. Williams, **Filled Skutterudite Antimonides: A New Class of Thermoelectric Materials**, Science **272**, 1325 (1996).
- [32] D. T. Morelli, G. P. Meisner, B. Chen, S. Hu, and C. Uher, **Cerium filling and doping of cobalt triantimonide**, Phys. Rev. B **56**, 7376 (1997).
- [33] C. Uher, J. Yang, S. Hu, D. T. Morelli, and G. P. Meisner, **Transport properties of pure and doped  $M\text{NiSn}$  ( $M=\text{Zr, Hf}$ )**, Phys. Rev. B **59**, 8615 (1999).
- [34] Q. Shen, L. Chen, T. Goto, T. Hirai, J. Yang, G. P. Meisner, and C. Uher, **Effects of partial substitution of Ni by Pd on the thermoelectric properties of  $\text{ZrNiSn}$ -based half-Heusler compounds**, Appl. Phys. Lett. **79**, 4165 (2001).
- [35] V. L. Kuznetsov, L. A. Kuznetsova, A. E. Kaliazin, and D. M. Rowe, **Preparation and thermoelectric properties of  $\text{A}_8^{\text{II}}\text{B}_{16}^{\text{III}}\text{B}_{30}^{\text{IV}}$  clathrate compounds**, J. Appl. Phys. **87**, 7871 (2000).
- [36] B. Wölfling, C. Kloc, J. Teubner, and E. Bucher, **High Performance Thermoelectric  $\text{Tl}_9\text{BiTe}_6$  with an Extremely Low Thermal Conductivity**, Phys. Rev. Lett. **86**, 4350 (2001).
- [37] D.-Y. Chung, T. Hogan, P. Brazis, M. Rocci-Lane, C. Kannevurf, M. Bastea, C. Uher, and M. G. Kanatzidis,  **$\text{CsBi}_4\text{Te}_6$ : A High-Performance Thermoelectric Material for Low-Temperature Applications**, Science **287**, 1024 (2000).
- [38] P. Larson, S. D. Mahanti, D.-Y. Chung, and M. G. Kanatzidis, **Electronic structure of  $\text{CsBi}_4\text{Te}_6$ : A high-performance thermoelectric at low temperatures**, Phys. Rev. B **65**, 045205 (2002).
- [39] B. C. Sales, **Smaller is Cooler**, Science **295**, 1248 (2002).
- [40] A. Majumdar, **Thermoelectricity in Semiconductor Nanostructures**, Science **303**, 777 (2004).
- [41] W. Kim, J. Zide, A. Gossard, D. Klenov, S. Stemmer, A. Shakouri, and A. Majumdar, **Thermal conductivity reduction and thermoelectric figure of merit increase by embedding nanoparticles in crystalline semiconductors**, Phys. Rev. Lett. **96**, 045901 (2006).
- [42] R. Venkatasubramanian, E. Siivola, T. Colpitts, and B. O'Quinn, **Thin-film thermoelectric devices with high room-temperature figures of merit**, Nature **413**, 597 (2001).

- [43] R. Venkatasubramanian, **Lattice thermal conductivity reduction and phonon localizationlike behavior in superlattice structures**, Phys. Rev. B **61**, 3091 (2000).
- [44] K. F. Hsu, S. Loo, F. Guo, W. Chen, J. S. Dyck, C. Uher, T. Hogan, E. K. Polychroniadis, and M. G. Kanatzidis, **Cubic  $\text{AgPb}_m\text{SbTe}_{2+m}$ : Bulk thermoelectric materials with high figure of merit**, Science **303**, 818 (2004).
- [45] E. Quarez, K. F. Hsu, R. Pcionek, N. Frangis, E. K. Polychroniadis, and M. G. Kanatzidis, **Nanostructuring, compositional fluctuations, and atomic ordering in the thermoelectric materials  $\text{AgPb}_m\text{SbTe}_{2+m}$ . The myth of solid solutions**, J. Am. Chem. Soc. **127**, 9177 (2005).
- [46] H. Lin, E. S. Božin, S. J. L. Billinge, E. Quarez, and M. G. Kanatzidis, **Nanoscale clusters in the high performance thermoelectric  $\text{AgPb}_m\text{SbTe}_{m+2}$** , Phys. Rev. B **72**, 174113 (2005).
- [47] D. Bilc, S. D. Mahanti, K.-F. Hsu, E. Quarez, R. Pcionek, and M. G. Kanatzidis, **Resonant states in the electronic structure of the high performance thermoelectrics  $\text{AgPb}_m\text{SbTe}_{2+m}$ : The role of Ag-Sb microstructures**, Phys. Rev. Lett. **93**, 146403 (2004).
- [48] J. Androulakis, K. F. Hsu, R. Pcionek, H. Kong, C. Uhr, J. J. D'Angelo, A. Downey, T. Hogan, and M. G. Kanatzidis, **Nanostructuring and high thermoelectric efficiency in  $p$ -Type  $\text{Ag}(\text{Pb}_{1-y}\text{Sn}_y)_m\text{SbTe}_{2+m}$** , Adv. Mater. **18**, 1170 (2006).
- [49] T. Egami and S. J. L. Billinge, *Underneath the Bragg peaks: structural analysis of complex materials*, Pergamon Press, Elsevier, Oxford, England, 2003.
- [50] S. J. L. Billinge and M. G. Kanatzidis, **Beyond crystallography: the study of disorder, nanocrystallinity and crystallographically challenged materials**, Chem. Commun. **2004**, 749 (2004).
- [51] R. Prinz and D. Koningsberger, editors, *X-ray absorption: principles, applications techniques of EXAFS, SEXAFS and XANES*, J. Wiley and Sons, New York, 1988.
- [52] S. P. Brown and L. Emsley, **Solid-State NMR**, in *Handbook of Spectroscopy*, edited by G. Gauglitz and T. Vo-Dinh, volume 2, Wiley, 2003.
- [53] V. M. Nield and D. A. Keen, *Diffuse Neutron Scattering from Crystalline Materials*, Oxford University Press, Oxford, England, 2001.
- [54] P. J. Chupas, X. Qiu, J. C. Hanson, P. L. Lee, C. P. Grey, and S. J. L. Billinge, **Rapid acquisition pair distribution function analysis (RA-PDF)**, J. Appl. Crystallogr. **36**, 1342 (2003).

- [55] P. J. Chupas, S. Chaudhuri, J. C. Hanson, X. Qiu, P. L. Lee, S. D. Shastri, S. J. L. Billinge, and C. P. Grey, **Probing local and long-range structure simultaneously: an in-situ study of the high-temperature phase transition of  $\alpha$ -AlF<sub>3</sub>**, J. Am. Chem. Soc. **126**, 4756 (2004).
- [56] A. P. Hammersley, **FIT2D v9.129 reference manual v3.1**, ESRF Internal Report ESRF98HA01T, 1998.
- [57] X. Qiu, J. W. Thompson, and S. J. L. Billinge, **PDFgetX2: a GUI driven program to obtain the pair distribution function from X-ray powder diffraction data**, J. Appl. Crystallogr. **37**, 678 (2004).
- [58] P. F. Peterson, M. Gutmann, T. Proffen, and S. J. L. Billinge, **PDFgetN: a user-friendly program to extract the total scattering structure function and the pair distribution function from neutron powder diffraction data**, J. Appl. Crystallogr. **33**, 1192 (2000).
- [59] S. J. L. Billinge, **Real-space Rietveld: full profile structure refinement of the atomic pair distribution function**, in *Local Structure from Diffraction*, edited by S. J. L. Billinge and M. F. Thorpe, page 137, New York, 1998, Plenum.
- [60] T. Proffen and S. J. L. Billinge, **PDFFIT, a program for full profile structural refinement of the atomic pair distribution function**, J. Appl. Crystallogr. **32**, 572 (1999).
- [61] C. L. Farrow, P. Juhas, J. W. Liu, D. Bryndin, E. S. Božin, J. Bloch, T. Proffen, and S. J. L. Billinge, **PDFfit2 and PDFgui: Computer programs for studying nanostructure in crystals**, J. Phys: Condens. Matter **19**, 335219 (2007).
- [62] M. Vershinin, S. Misra, S. Ono, Y. Abe, Y. Ando, and A. Yazdani, **Local ordering in the pseudogap state of the high- $T_c$  superconductor Bi<sub>2</sub>Sr<sub>2</sub>CaCu<sub>2</sub>O<sub>8+ $\delta$</sub>** , Science **303**, 1995 (2004).
- [63] J. E. Hoffman, E. W. Hudson, K. M. Lang, V. Madhavan, H. Eisaki, S. Uchida, and J. C. Davis, **A four unit cell periodic pattern of quasi-particle states surrounding vortex cores in Bi<sub>2</sub>Sr<sub>2</sub>CaCu<sub>2</sub>O<sub>8+ $\delta$</sub>** , Science **295**, 466 (2002).
- [64] T. Hanaguri, C. Lupien, Y. Kohsaka, D. H. Lee, M. Azuma, M. Takano, H. Takagi, and J. C. Davis, **A ‘checkerboard’ electronic crystal state in lightly hole-doped Ca<sub>2-x</sub>Na<sub>x</sub>CuO<sub>2</sub>Cl<sub>2</sub>**, Nature **430**, 1001 (2004).
- [65] J. C. Loudon, S. Cox, A. J. Williams, J. P. Attfield, P. B. Littlewood, P. A. Midgley, and N. D. Mathur, **Weak charge-lattice coupling requires reinterpretation of stripes of charge order in La<sub>1-x</sub>Ca<sub>x</sub>MnO<sub>3</sub>**, Phys. Rev. Lett. **94**, 097202 (2005).
- [66] G. C. Milward, M. J. Calderon, and P. B. Littlewood, **Electronically soft phases in manganite**, Nature **433**, 607 (2005).

- [67] D. E. Moncton, F. J. Disalvo, J. A. Wilson, B. G. Bagley, and J. V. Waszczak, **Effects of doping on charge-density waves in layer compounds**, Phys. Rev. B **12**, 2220 (1975).
- [68] H. P. Hughes and R. A. Pollack, **Charge-density wave phases in 1T-TaS<sub>2</sub> and 1T-TaSe<sub>2</sub> observed by x-ray photoemission**, Commun. Phys. **1**, 61 (1976).
- [69] B. H. Suits, S. Couturie, and C. P. Slichter, **Confirmation of McMillan concept of discommensurations**, Phys. Rev. Lett. **45**, 194 (1980).
- [70] B. H. Suits, S. Couturie, and C. P. Slichter, **NMR test of McMillan concept of discommensurations in 2H-TaSe<sub>2</sub>**, Phys. Rev. B **23**, 5142 (1981).
- [71] C. H. Chen, J. M. Gibson, and R. M. Fleming, **Direct observation of charge density wave discommensurations and dislocations in 2H-TaSe<sub>2</sub>**, Phys. Rev. Lett. **47**, 723 (1981).
- [72] J. M. Gibson, C. H. Chen, and M. L. McDonald, **Ultrahigh-resolution electron microscopy of charge-density waves in 2H-TaSe<sub>2</sub> below 100K**, Phys. Rev. Lett. **50**, 1403 (1983).
- [73] T. Ishiguro and H. Sato, **Electron-microscopy of phase-transformations in 1T-TaS<sub>2</sub>**, Phys. Rev. B **44**, 2046 (1991).
- [74] M. Kuwabara, M. Tomita, H. Hashimoto, and H. Endoh, **Direct observation of the superstructure of the nearly commensurate phase in 1T-TaS<sub>2</sub> by high-resolution electron-microscopy**, Phys. Status Solidi A **96**, 39 (1986).
- [75] J. W. Steeds, D. M. Bird, D. J. Eaglesham, S. McKernan, R. Vincent, and R. L. Withers, **Study of modulated structures by transmission electron microscopy**, Ultramicroscopy **18**, 97 (1985).
- [76] R. E. Thomson, B. Burk, A. Zettl, and J. Clarke, **Scanning-tunneling-microscopy of the charge-density-wave structure in 1T-TaS<sub>2</sub>**, Phys. Rev. B **49**, 16899 (1994).
- [77] W. Lin, H. Steinfink, and E. J. Weiss, **The phase equilibria and crystal chemistry of the rare earth group VI systems. III. neodymium-tellurium**, Inorg. Chem. **4**, 877 (1965).
- [78] E. DiMasi, M. C. Aronson, J. F. Mansfield, B. Foran, and S. Lee, **Chemical pressure and charge-density waves in rare-earth tritellurides**, Phys. Rev. B **52**, 14516 (1995).
- [79] C. Malliakas, S. J. L. Billinge, H.-J. Kim, and M. G. Kanatzidis, **Square nets of tellurium: Rare-earth dependent variation in the charge-density wave of RETe<sub>3</sub> (RE= rare earth element)**, J. Am. Chem. Soc. **127**, 6510 (2005).





- [80] G. H. Gweon, J. D. Denlinger, J. A. Clack, J. W. Allen, C. G. Olson, E. Di-Masi, M. C. Aronson, B. Foran, and S. Lee, **Direct observation of complete Fermi surface, imperfect nesting, and gap anisotropy in the high-temperature incommensurate charge-density-wave compound  $\text{SmTe}_3$** , Phys. Rev. Lett. **81**, 886 (1998).
- [81] V. Brouet, W. L. Yang, X. J. Zhou, Z. Hussain, N. Ru, K. Y. Shin, I. R. Fisher, and Z. X. Shen, **Fermi surface reconstruction in the CDW state of  $\text{CeTe}_3$  observed by photoemission**, Phys. Rev. Lett. **93**, 126405 (2004).
- [82] H. Komoda, T. Sato, S. Souma, T. Takahashi, Y. Ito, and K. Suzuki, **High-resolution angle-resolved photoemission study of incommensurate charge-density-wave compound  $\text{CeTe}_3$** , Phys. Rev. B **70**, 195101 (2004).
- [83] J. Laverock, S. B. Dugdale, Z. Major, M. A. Alam, N. Ru, I. R. Fisher, G. Santi, and E. Bruno, **Fermi surface nesting and charge-density wave formation in rare-earth tritellurides**, Phys. Rev. B **71**, 085114 (2005).
- [84] A. P. Hammersley, S. O. Svenson, M. Hanfland, and D. Hauserman, **Two-dimensional detector software: from real detector to idealised image or two-theta scan**, High Pressure Res. **14**, 235 (1996).
- [85] R. Patschke and M. G. Kanatzidis, **Polytelluride compounds containing distorted nets of tellurium**, Phys. Chem. Chem. Phys. **4**, 3266 (2002).
- [86] R. Patschke, J. D. Breshears, P. Brazis, C. R. Kannewurf, S. J. L. Billinge, and M. G. Kanatzidis,  **$\text{Cu}_x\text{UTe}_3$ : Stabilization of  $\text{UTe}_3$  in the  $\text{ZrSe}_3$  Structure Type via Copper Insertion. The Artifact of Te-Te Chains and Evidence for Distortions Due to Long Range Modulations**, J. Am. Chem. Soc. **123**, 4755 (2001).
- [87] J. Nylén, M. Andersson, S. Lidin, and U. Häussermann, **The Structure of  $\alpha\text{-Zn}_4\text{Sb}_3$ : Ordering of the Phonon-Glass Thermoelectric Material  $\beta\text{-Zn}_4\text{Sb}_3$** , J. Am. Chem. Soc. **126**, 16306 (2004).
- [88] T. Caillat, J.-P. Fleurial, and A. Borshchevsky, **Preparation and Thermoelectric Properties of Semiconducting  $\text{Zn}_4\text{Sb}_3$** , J. Phys. Chem. Solids **58**, 1119 (1997).
- [89] G. J. Snyder, M. Christensen, E. Nishibori, T. Caillat, and B. B. Iversen, **Disordered zinc in  $\text{Zn}_4\text{Sb}_3$  with phonon-glass and electron-crystal thermoelectric properties**, Nature Mater. **3**, 458 (2004).
- [90] S. Schlecht, C. Erk, and M. Yosef, **Nanoscale Zinc Antimonides: Synthesis and Phase Stability**, Inorg. Chem. **45**, 1693 (2006).
- [91] C. Kittel, *Introduction to Solid State Physics 7th edition*, John Wiley & Sons, Inc, New York, USA, 1996.

- [92] Y. Mozharivskyj, A. O. Pecharsky, S. Bud'ko, and G. J. Miller, **A Promising Thermoelectric Material:  $\text{Zn}_4\text{Sb}_3$  or  $\text{Zn}_{6-\delta}\text{Sb}_5$ . Its Composition, Structure, Stability, and Polymorphs. Structure and Stability of  $\text{Zn}_{1-\delta}\text{Sb}$** , Chem. Mater. **16**, 1580 (2004).
- [93] H. W. Mayer, I. Mikhail, and K. Schubert, **Phases of  $\text{ZnSb}_N$  and  $\text{CdSb}_N$  mixtures**, Journal of the Less Common Metals **59**, 43 (1978).
- [94] F. Cargnoni, E. Nishibori, P. Rabiller, L. Bertini, G. J. Snyder, M. Christensen, C. Gatti, and B. B. Iversen, **Interstitial Zn Atoms Do the Trick in Thermoelectric Zinc Antimonide,  $\text{Zn}_4\text{Sb}_3$ : A combined Maximum Entropy Method X-ray Electron Density and Ab Initio Electronic Structure Study**, Chem.-Eur. J. **10**, 3862 (2004).
- [95] A. S. Mikhaylushkin, J. Nylén, and U. Häussermann, **Structure and Bonding of Zinc Antimonides: Complex Frameworks and Narrow Band Gaps**, Chem.-Eur. J. **11**, 4912 (2005).
- [96] B. C. Sales, B. Chakoumakos, D. Mandrus, and J. W. Sharp, **Atomic displacement parameters and the lattice thermal conductivity of clathrate-like thermoelectric compounds**, J. Solid State Chem. **146**, 528 (1999).
- [97] M. D. N. Regueiro, J. M. Lopez-Castillo, and C. Ayache, **Thermal Conductivity of  $1T\text{-TaS}_2$  and  $2H\text{-TaSe}_2$** , Phys. Rev. Lett. **55**, 1931 (1985).
- [98] E. Dagotto, **Complexity in strongly correlated electronic systems**, Science **309**, 257 (2005).
- [99] X. Qiu, Th. Proffen, J. F. Mitchell, and S. J. L. Billinge, **Orbital correlations in the pseudocubic  $O$  and rhombohedral  $R$ -phases of  $\text{LaMnO}_3$** , Phys. Rev. Lett. **94**, 177203 (2005).
- [100] L. E. Cross, **Relaxor ferroelectrics**, Ferroelectrics **76**, 241 (1987).

MICHIGAN STATE UNIVERSITY LIBRARIES



3 1293 02956 3156